Challenge Journal of
STRUCTURAL MECHANICS

Vol.3 No.3 (2017)

North Anatolian Fault Zone Poisson method building codes columns continuous girder bridge corrosion durability dynamic analysis dynamic response earthquake earthquake hazard finite element analysis finite element method optimization reinforced concrete seismic analysis seismic design seismic isolation seismic response teaching-learning based optimization wind

TULPAR ACADEMIC PUBLISHING

ISSN 2149-8024

Challenge Journal of Structural Mechanics

E-mail: *cjsmec@challengejournal.com*

Web page: *cjsmec.challengejournal.com*

TULPAR Academic Publishing
www.tulparpublishing.com

Challenge Journal of Structural Mechanics

CONTENTS

TULPAR ACADEMIC PUBLISHING

Challenge Journal of Structural Mechanics

Modal identification of a reduced-scale masonry arch bridge with experimental measurements and finite element method

Emre Alpaslan [a,*], Burcu Dinç [a], Kemal Hacıefendioğlu [a], Gökhan Demir [a], Olgun Köksal [b]

[a] *Department of Civil Engineering, Ondokuz Mayıs University, 55139, Samsun, Turkey*
[b] *Kavak Vocational School, Ondokuz Mayıs University, 55850 Samsun, Turkey*

ABSTRACT

This study aims to investigate modal parameters such as mode shapes, natural frequencies and damping ratios of a reduced scale one-span historical masonry arch bridge constructed in laboratory conditions by performing numerical and experimental analysis. Sarp Dere historical masonry bridge, in Ordu, Ulubey, has 15.5 m in length and 4.75 m in width was chosen as a prototype model. The reduced-scale bridge model and structural details were carried out in the scale of 1:12.5. Operational Modal Analysis (OMA) technique was used for experimental study. The experimental modal parameters of the bridge model were figured out by using Enhanced Frequency Domain Decomposition (EFDD). ANSYS software was used to create 3D finite element (FE) model and to expose the analytical modal parameters of the reduced-scaled bridge model. Moreover, FE model of the reduced-scale bridge model was calibrated based on the experimental results by using the Response Surface based FE model calibration technique to obtain more accurate results. The analysis results of experimental, initial and calibrated FE model were compared. It is noted that there are significant differences between the modal parameters obtained from experimental and initial FE model. Model calibration techniques are beneficial to get a more reasonable FE model.

ARTICLE INFO

Article history:
Received 17 February 2017
Revised 5 June 2017
Accepted 22 June 2017

Keywords:
Operational modal analysis
Reduced-scale model
Finite element model
Historical masonry arch bridge

1. Introduction

Historical masonry structures have significant valuable for countries due to reflecting their heritage and culture. One the most important masonry structures are masonry arch bridges generally used as a primitive railway infrastructure. Masonry arch bridges can have various styles, sizes and spans. These structures have social, economic and strategic importance; therefore, masonry arch bridge must be repaired, strengthened and protected. Historical masonry arch bridges are exposed to the dynamic loadings of traffic, wind and earthquakes. Therefore, it is critical to determine the modal parameters (such as natural frequencies, mode shapes and damping ratios) of these kinds of structures.

Due to importance of masonry structures for historical point of view, many researches have focused on methods including both experimental and analytical investigations to understand dynamic behavior of these types of structures. AVT Ambient Vibration Test (AVT) or Operational Modal Analysis (OMA) method is one of the most suitable and efficiency method to experimentally determine the modal parameters of these kinds of structures because it is a non-destructive method. Furthermore, these kinds of structures have complicated geometry and uncertain material properties and boundary conditions; therefore, it is difficult to obtain finite element (FE) model of these kinds of structures that truly reflects modal parameters. Thus, FE model generally needs calibration techniques. The procedure includes that modifies or updates the uncertainty parameters in the initial finite element model according to experimental test results to achieve more accurate structural numerical model according to the study done by Friswell MI and Mottershead JE (1995).

* *Corresponding author*. Tel.: +90-362-3121919 ; E-mail address: emre.alpaslan@omu.edu.tr (E. Alpaslan)
ISSN: 2149-8024 / DOI: https://doi.org/10.20528/cjsmec.2017.06.012

Bayraktar et al. (2009) investigated the dynamic characteristics of the Hagia Sophia bell-tower located in Trabzon, Turkey by using ambient vibration test and operational modal analysis. The modal parameters of the structure were obtained and compared the finite element analysis results. While there are some differences between natural frequencies, a good agreement is achieved between mode shapes. Foti et al. (2012) performed an experimental test on a bell tower to investigate the dynamic structural behaviour of slender masonry structure. Operational modal analysis was performed for experimental works. The main frequencies and damping ratios were obtained from measurements at some relevant locations. Finite element model of the structure was developed and the analysis results compared the experimental results. The initial mechanical values of the structure were calibrated following an iterative approach until a good harmony between numerical and experimental frequencies were achieved. Gentile et al. (2015) investigated the modal parameters of the historic bell tower of the church and got the ambient response of the structure. For operational modal analysis, the study used stochastic subspace identification method. The finite element model of the structure was updated according to the experimental results and calibration procedure consisted of systematic manual tuning, sensitivity analysis, and simple system identification algorithm. After the calibration procedure, the differences between modal parameters of the experimental and finite element analysis results did not exceed %1.20 and enough correlation in terms of mode shapes was acquired.

The study done by Çalık et al. (2014) related to investigation of the dynamic characteristics of the masonry vault of Küçük Fatih Mosque by using Ambient Vibration Test. The natural frequencies, mode shapes and the modal damping ratios of the damaged and restored structure were identified by measuring the vibrational responses of the vault under environmental effects. It is concluded that the first five natural frequencies of the damaged and restored vault increased and damping ratios varied irregularly. Sevim et al. (2011) examined importance of model calibration effects on the earthquake response of masonry arch bridges by using OMA. Modal analysis results of finite element models of Osmanlı and Senyuva historical arch bridges were calibrated according to the in situ modal test results. Earthquake excitation recorded during the Erzincan Earthquake in 1992 was applied to initial and adjusted finite element model of two historical arch bridges and demonstrated the importance of model calibration and ambient vibration testing. Brencich and Sabia (2008) examined Tanaro Bridge constructed in 1866. Dynamic test was performed and natural frequencies, damping ratios and mode shapes of the historical bridge were obtained. The study performed by Bayraktar et al. (2010) is about analytical modelling, modal testing, and finite element model updating for a two-span masonry arch bridge. The results demonstrated that maximum differences in the natural frequencies are decreased on average from 18 to 7% and a good agreement is achieved between analytical and experimental dynamic characteristics after finite element model updating. Nohutcu et al. (2015) investigated the numerical and experimental modal parameters of a historical mosque called Hafsa Sultan in Manisa, Turkey by using FE method and OMA, respectively. Because there were some differences between natural frequencies between FE model and OMA, the finite element model of the structure was calibrated based on the results obtained from ambient vibration test by changing material parameters. More realistic numerical model of the mosque was obtained after calibration process.

A few studies have focused on the response surface method for the structural finite element model calibration in the civil engineering field such as Xin et al. (2015), Marcin et al. (2014), and Zhouhong et al. (2015). Ren and Chen (2010) presented the procedure by a simulated simply supported beam and a full-size precast continuous box girder bridge tested under operational vibration conditions. The results compared with those determined from the traditional sensitivity-based FE model calibration method. It is presented that the model calibration process becomes efficient and converges fast compared with the traditional sensitivity-based model calibration method. The study concluded that the response surface-based FE model calibration procedure is easy and fast to be implemented in practice. Deng and Cai (2010) studied model updating procedure by using response surface method. They used simply supported beam as a numerical example. Also, they applied this method to the model updating of an existing bridge. The study concluded that response surface method works well and obtain reasonable physical explanations for the updated parameters.

This study deals with investigating effectivity of response surface-based finite element model calibration method for historical masonry arch bridges. For this purpose, a reduced-scale model of Sarp Dere historical masonry bridge was built in laboratory conditions and its modal parameters were investigated. Finite element model of the scaled bridges was developed in ANSYS and experimental results were compared with the initial finite element model of the bridge. Calibration of the finite element model was utilized depending on the Operational Modal Analysis results of the reduced-scale model of the bridge by using the response surface-based finite element model calibration method. Correlation studies were conducted between the experimental and analytical modal parameters results of the reduced-scaled historical masonry arch bridge to minimize the uncertain finite element modeling parameters such as material properties and boundary conditions. For future study, the effects of damaged and repaired reduced-scale bridge model on the modal parameters can be investigated by using response surface-based model calibration technique according to the results obtained in this study.

2. Formulation

In general, Enhanced frequency domain decomposition (EFDD) technique is used for Operational Modal Analysis in the civil engineering industries. In the EFDD technique, the spectral density matrix is approximately

separated into a set of single degree of freedom (SDOF) systems utilizing the Singular Value Decomposition. It is possible to get exact results in the case where loading is white noise, the structure is lightly damped, and if the mode shapes of close modes are geometrically orthogonal. Even if these assumptions are not satisfied, the results are significantly reasonable according to Brincker et al. (2000) The relationship between unknown input $x(t)$ and the measured responses $y(t)$ is expressed based on Ewins (1984) and Bendat and Piersol (2004) as;

$$\left[G_{yy}(jw)\right] = [H(jw)]^{*}[G_{xx}(jw)][H(jw)]^{T}, \quad (1)$$

where $G_{xx}(jw)$ is the power spectral density (PSD) matrix of the input, $G_{yy}(jw)$ is the PSD matrix of the responses, $H(jw)$ is the frequency response function (FRF) matrix, and * and superscript T donate complex conjugates and transpositions, respectively.

3. Application

In this study, Sarp Dere historical masonry arch bridge has 15.5m in length and 4.75m in width was considered as a prototype model. The historical bridge is one-span masonry bridge which carries Ottoman architectural features. The main line of the arch consists of 47 stones and the side walls of the bridge have 50 cm width. Restoration of the bridge was completed in 2012 under the supervision of the 7th Regional Directorate of Highways. Figs. 1(a-d) present the masonry bridge and its geometrical properties. A reduced-scaled model of the one-span historical bridge was constructed in laboratory conditions to estimate the dynamic characteristics of the prototype bridge model, which are natural frequencies, mode shapes and damping ratios. The model and structural details including masonry bricks, mortar joints and filling material were implemented in the scale 1:12.5. The scaled bridge model has 159 cm in length and 36 cm in width. The bridge model was consisted of arch, side walls, filling material and parapets. Gas concrete also known as autoclaved aerated concrete was used as a construction material of the arch, side walls and parapets. According to Turkish Standards (TSE 453), autoclaved aerated concrete is a porous lightweight concrete produced by the mixture of fine grain siliceous aggregate and an inorganic binder (lime and/or cement). In the production procedure, its unit weight is decreased by adding a pore-forming agent and it is exposed steam curing to provide its mechanical strength. The reason of the material choice is to be comforted with geometrical scale proportion of the model bridge elements due to its ability of workability. Modulus of elasticity of autoclaved aerated concrete has been given as a function of the density and compressive strength of the material. The modulus of elasticity for a autoclaved aerated concrete having a density range of 500 to 700 kg/m^3 was reported to be 1.4 to 2.8 103 MPa according to MacElroy and Kimpflen (1990). Each gas concrete elements were immersed in mortar mixture to be able to obtain appropriate mechanical properties comply with the prototype bridge elements. The filling material is natural soil with %10 chaffy. The mechanical properties of the construction material are shown in Table 1. The arch of the historical bridge model is formed as various curvatures, four different radius and central angle and includes total 47 stone. The side walls have 4 cm in width on both downstream and upstream sides. Horosan mortar consisting of brick-dust and lime paste was used as a fastener material of the construction elements. The scaled bridge model was supported by two separate abutment composed of the mixture of the cement paste and gas concrete. Fig. 1(e) demonstrates the reduced scale bridge model.

3.1. Modal test and experimental modal parameters

Operational modal analysis was carried out to determine dynamic characteristics of reduced scale bridge model. One-axial accelerometers and data acquisition system were used to get signals obtained from small artificial vibrations in order to vibrate the reduced-scaled bridge model for the experimental measurements. 12 accelerometers were utilized in total and were put into six different locations on both Y and Z direction on the span of the bridge model. Fig. 2 represents the test setup of experimental study of the reduced-scaled bridge model. Moreover, one reference accelerometer was disposed on the middle point of the span in order to combine the six measurement data taken in each axis. The signals gathering from accelerometers were obtained by using data acquisition network access software Testlab_V2. Measurement duration was chosen as 15 minutes and the frequency range was taken as 0-50 Hz. The data collected from the accelerometers corresponding to specified points are illustrated in Fig. 3. ARTeMIS 1.5 software (2013) was performed to obtain the experimental modal parameters of the reduced-scale historical masonry bridge model. The natural frequencies, modal damping ratios and mode shapes of the scaled bridge model were procured by performing EFDD technique. The signal time series for all channels and the singular values of spectral density matrices of data set obtained from the EFDD technique are demonstrated in Figs. 4 and 5, respectively. Furthermore, experimentally obtained natural frequencies and mode shapes of first three modes of the scaled bridge model are shown in Fig. 6. The first three mode shapes of the reduced-scale bridge model can be expressed as lateral mode in y-direction for the first mode and transverse modes for second and third modes.

Table 1. Mechanical properties of construction materials.

	Unit Weight (g/cm^3)	Modulus of Elasticity (N/mm^2)	Poisson's Ratio
Gas concrete	0.800	1600	0.20
Chaffy soil	1.365	1500	0.05

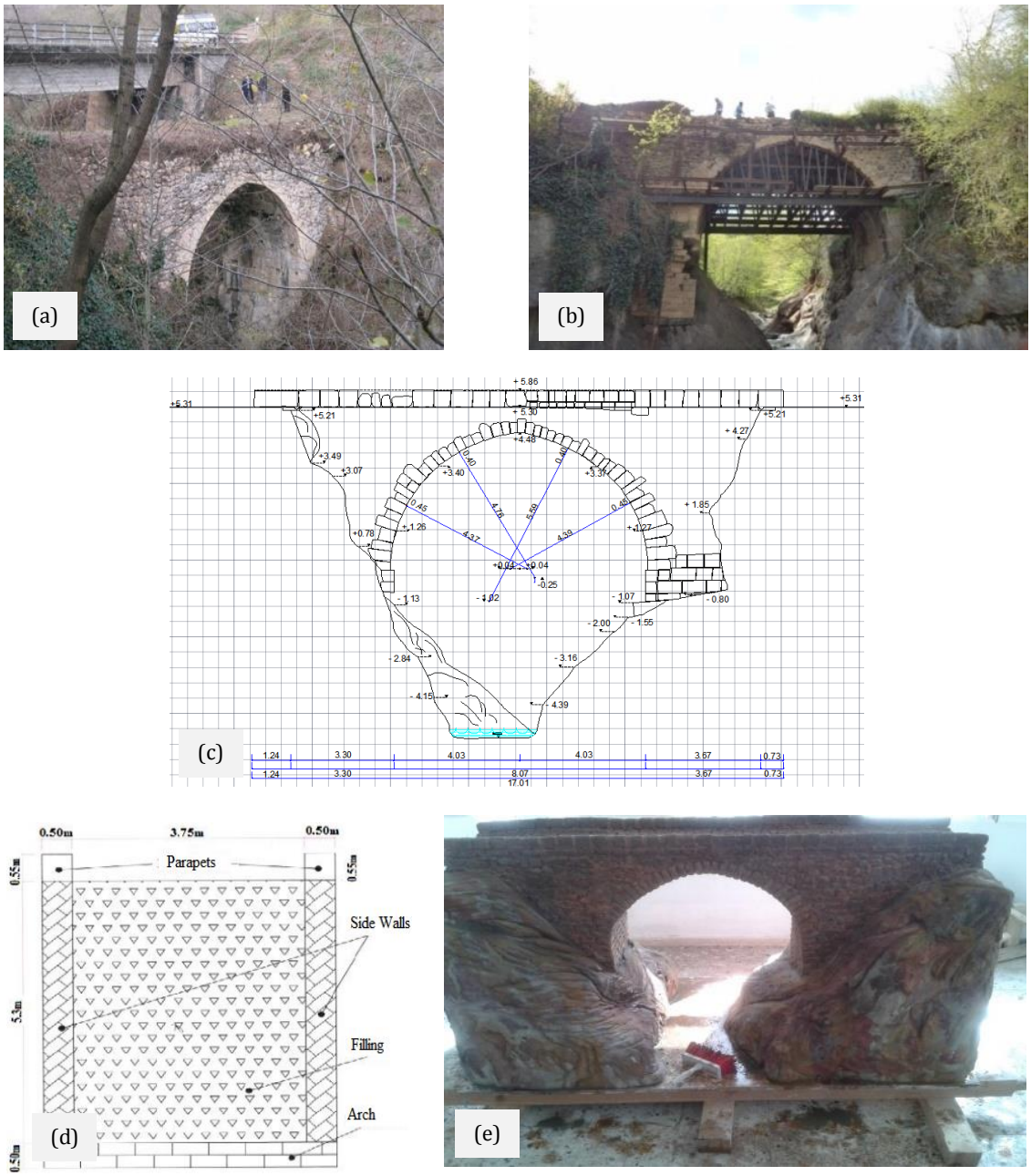

Fig. 1. (a) Sarp Dere Bridge; (b) Restoration of the Bridge; (c) Longitudinal cross-section of prototype bridge (the unities are in m); (d) Transverse cross section of prototype bridge; (e) Reduced scale bridge model.

Fig. 2. Test setup of reduced-scaled bridge model.

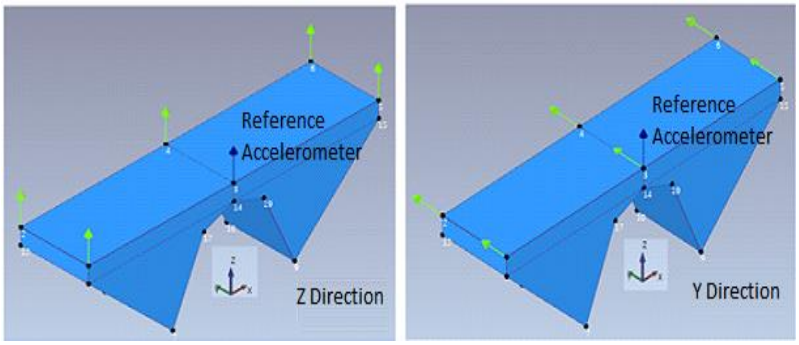

Fig. 3. Configuration of the accelerometers.

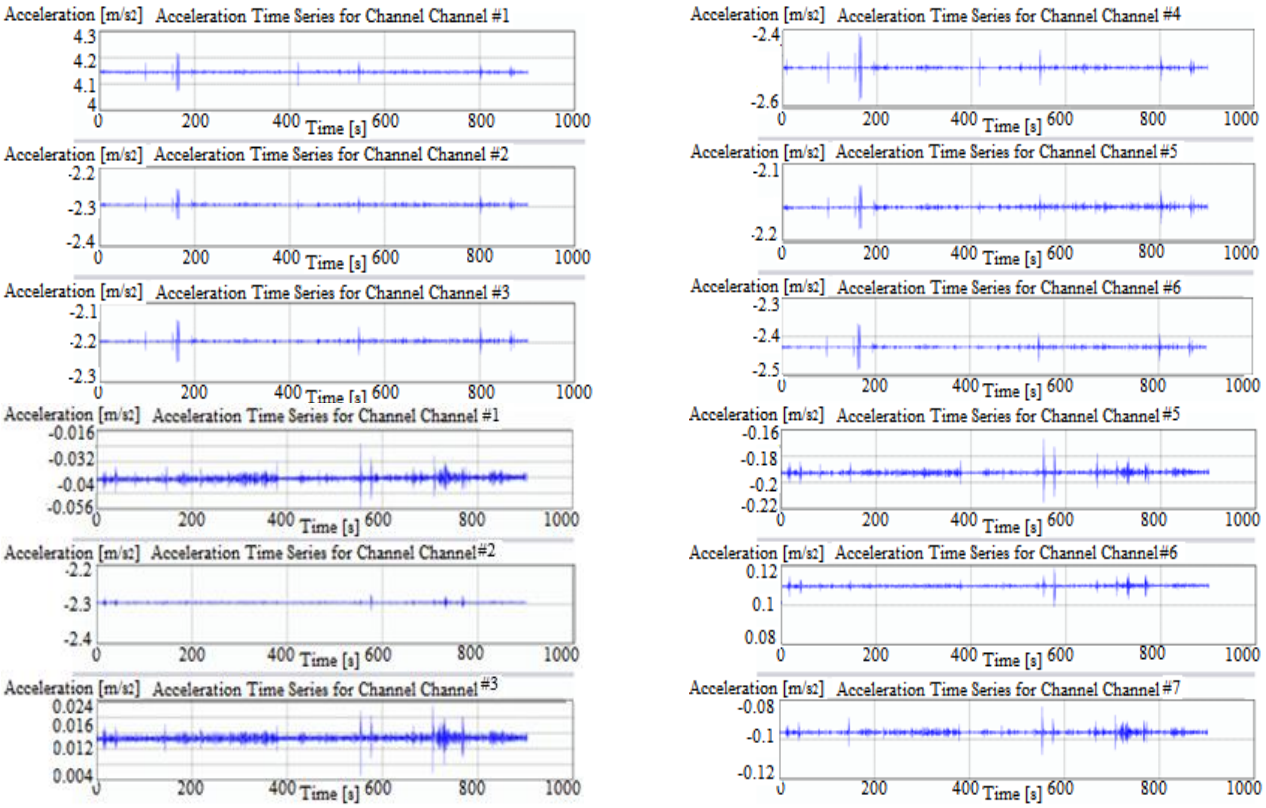

Fig. 4. Signal time series for channels.

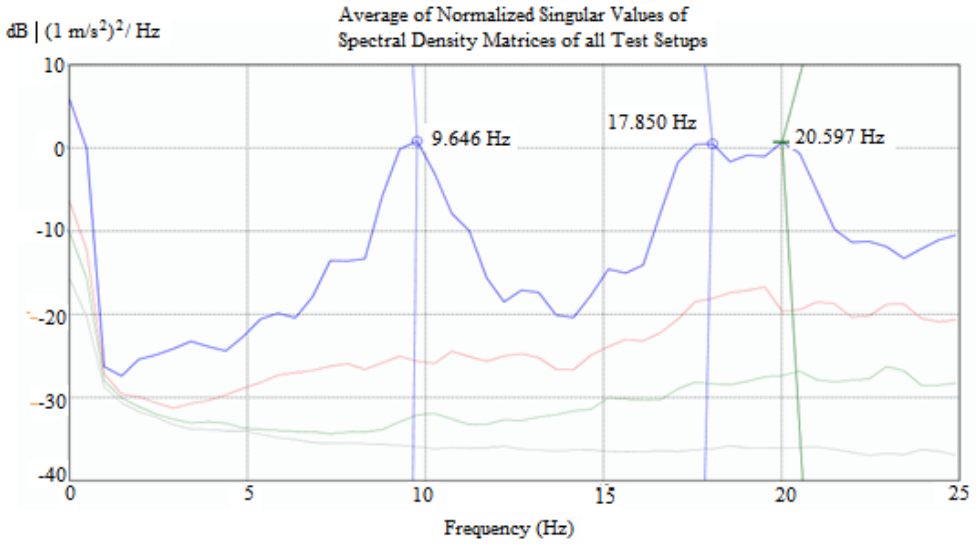

Fig. 5. Average of normalized singular values of spectral density matrices of all test setups.

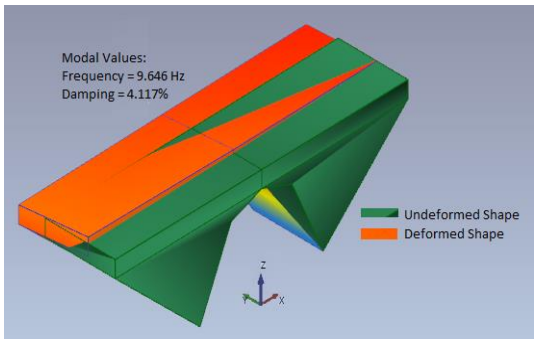

(a) Mode 1 (lateral mode)

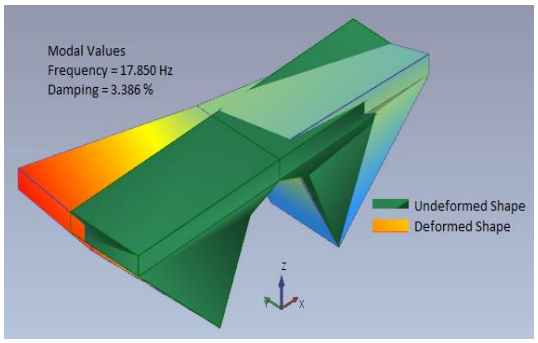

(b) Mode 2 (1st transverse mode)

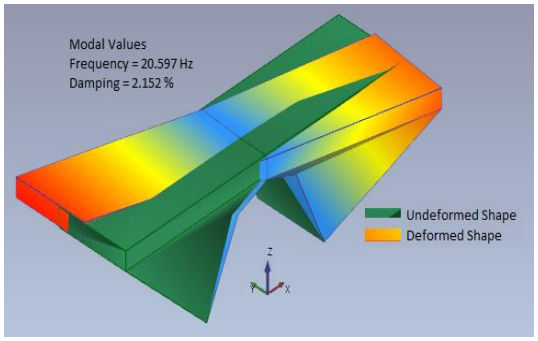

(c) Mode 3 (2nd transverse mode)

Fig. 6. Experimentally identified first three mode shapes of the scaled bridge model.

3.2. Finite element modelling

Three dimensional finite element model of scaled bridge model was created in ANSYS (2013) software to evaluate the dynamic characteristics of the bridge which are natural frequencies and natural mode shapes. SOLID186 elements for the three-dimensional modelling of solid structures were used to model the bridge model. This element is defined by 20 nodes; each node has 3 translational degrees of freedom, namely, u_x, u_y and u_z. It supports plasticity, hyperelasticity, creep, swelling, stress stiffening, large deflection, and large strain capabilities (ANSYS 2013). The mechanical properties of the scaled bridge model, the modulus of elasticity, Poisson's ratio and mass density, were used as shown in Table 1. In the model, linear elastic material behaviour is assumed and the stiffness degradation is neglected. The finite element model of the scaled bridge includes 21854 solid elements and 113250 nodes in total. The three dimensional FE model of the scaled bridge created using section properties of the prototype bridge. The boundary conditions of the FE model of the bridge were created as reduced-scale bridge model. In the FE model, the bridge supported on two abutments on two sides and the model was sit on a platform as illustrated in Fig. 7. For initial FE model, it was assumed that boundary condition of the bridge's foundation was assumed to be rigid; therefore, all of the degrees of freedoms under the platform of the bridge model were accepted as fix support.

3.3. Finite element model calibration

The natural frequencies and modal shapes of the reduced-scaled bridge model were computed from the finite element analysis according to the initial mechanical parameters and boundary conditions as indicated in Section 3.2. The natural frequencies obtained from the initial conditions are shown in Table 2. It can be realized that there are significant differences between the frequencies obtained from analytical and experimental analyses according to the initial conditions.

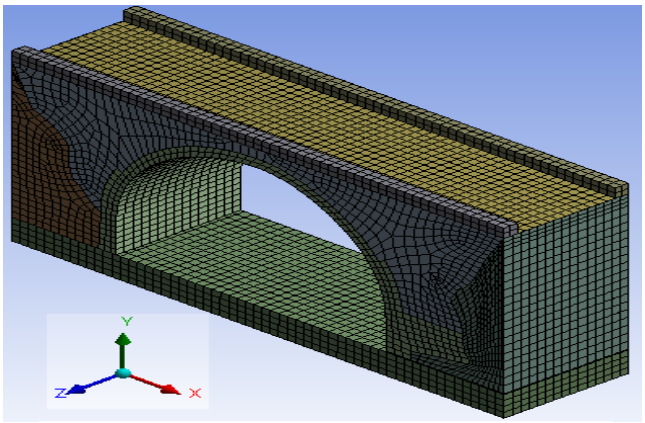

Fig. 7. Finite element model of the scaled bridge model.

These differences may due to uncertainties elastic mechanical properties of materials, inaccurate boundary conditions and assumptions of structural geometry. Therefore, the FE model calibration should be performed to achieve more accurate results. The material properties and boundary conditions of finite element model can be changed in order to calibrate the modal parameters of finite element model and get more accurate results reflected the dynamic behaviour of reduced-scaled bridge model. In this study, the elastic mechanical properties of boundary conditions (abutments) of finite element model were changed. Moreover, the platform under the bridge was modelled by a flexible boundary, which permits a more flexible dynamic behaviour of the structure. During the calibration process, the material properties of reduced-scale bridge model (the elastic modulus, unit weight and Poisson's ratio) were not changed.

The manual or automatic model calibration methods are benefited in many studies. In this study, the response surface-based FE model calibration for OMA was applied to the reduced-scaled historical masonry bridge. Natural frequencies evaluated from Eigen analysis of the FE model were compared to the experimental analysis; the optimal results were found using the optimizations

method based on Casciati (2010). The aim of this method is to close the gap between the numerical results and the experimental ones. The frequencies obtained from the analytical analyses which are for before and after calibration and experimental modal parameters are shown in Table 2. The differences of the first three modal frequencies for experimental and initial FE model varied between 0.3 - 5.8%. After model calibration, the differences of modal frequencies for experimental and calibrated FE model decreased to 0.2 – 0.8%. Model calibration technique demonstrated that the natural frequencies computed from the FE method show a good compatibility with those found from EFDD technique. The analytically defined first three mode shapes of the bridge are demonstrated in Fig. 8. It can be seen that there is enough agreement between mode shapes when the analytical and experimental results are compared with each other. Furthermore, the first three damping ratios of the reduced scale historical masonry bridge model identified as 2.15 – 4.12% using ARTeMIS Modal Pro 1.5.

Table 2. Analytical and experimental modal parameters.

	Initial finite element model	Calibrated finite element model	Experimental modal analysis		Differences	
					Initial finite element model	Calibrated finite element model
Modes	Frequency (Hz)	Frequency (Hz)	Frequency (Hz)	Damping ratio (%)	(%)	(%)
1	10.21	9.67	9.65	4.12	5.8	0.2
2	16.64	17.71	17.85	3.39	6.8	0.8
3	20.53	20.64	20.60	2.15	0.3	0.2

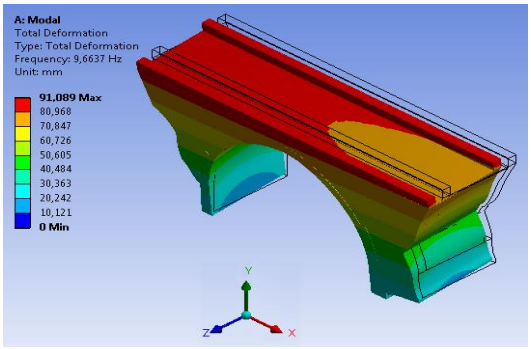

(a) Mode 1 (9.67 Hz)

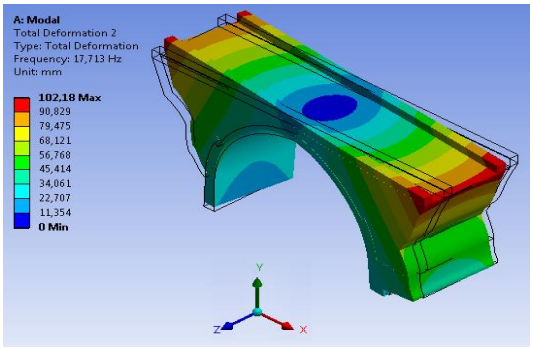

(b) Mode 2 (17.71 Hz)

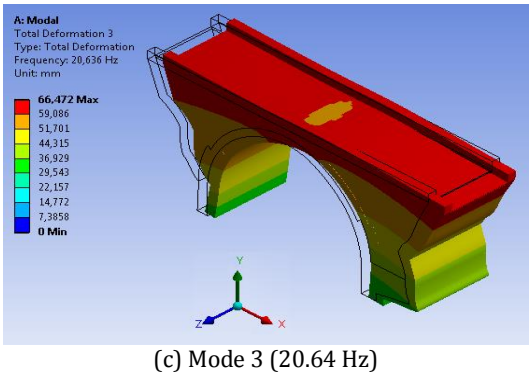

(c) Mode 3 (20.64 Hz)

Fig. 8. Analytically identified first three mode shapes of the scaled bridge model.

4. Conclusions

In this study, modal parameters of a reduced-scale historical masonry bridge were investigated by using the Operational modal analysis. In accordance with this purpose, Sarp Dere historical masonry arch bridge located in Ordu was selected as a prototype model. The Operational Modal Analysis test is realized under environmental vibration. The Enhance Frequency Domain Decomposition (EFDD) method is used to define the natural frequencies, mode shapes and damping ratios experimentally. 3D finite element model of historical masonry bridge is modelled ANSYS software and detected the natural frequencies and mode shapes analytically.

Experimental and analytical results with the initial conditions were compared and significant differences were observed. For this reason, response surface-based FE model calibration technique was utilized to close the frequencies obtained from the analytical analysis to those of experimental analysis. Following are conclusions from this study:

- It was seen from the analytical results that the first three natural frequencies are in the range between 10 Hz and 20 Hz.
- The experimentally determined first three damping ratios of the reduced-scale historical masonry bridge model was range of 2.15% to 4.12%.
- The first three mode shapes of the reduced-scale bridge model can be classified as lateral mode and transverse modes. Similar mode shapes were obtained from the numerical analysis.
- The first and second analytical frequencies according to the initial conditions demonstrated significant differences compared to the experimental frequencies.
- Response surface-base FE calibration was performed to close the differences between natural frequencies obtained from experimental and numerical analysis.
- Calibration of the finite element model by using response surface method is seen as a good approach to

- Response surface-base FE calibration was performed to close the differences between natural frequencies obtained from experimental and numerical analysis.
- Calibration of the finite element model by using response surface method is seen as a good approach to determine to modal parameters of reduced-scale historical masonry bridges. After the finite element model calibration, the differences between experimental and analytical natural frequencies declined considerably.

According to the results obtained in this study, it is aimed to investigate the functionality of response surface-based FE model calibration technique to obtain modal parameters of damaged and repaired reduced-scale historical masonry bridge model for future study.

REFERENCES

ANSYS, Release 14.5 (2013). ANSYS , Inc., Canonsburg, PA, USA.

Bayraktar A, Türker T, Sevim B, Altunışık AC, Yıldırım F (2009). Modal parameter identification of Hagia Sophia Bell-Tower via ambient vibration test. *Journal of Nondestructive Evaluation*, 28(1), 37-47.

Bayraktar A, Altunişik AC, Birinci F, Sevim B, Türker T (2010). Finite-element analysis and vibration testing of a two-span masonry arch bridge. *Journal of Performance of Constructed Facilities*, 24(1) 46-52.

Bendat JS, Piersol AG (2004). Random Data: Analysis and Measurement Procedures. John Wiley and Sons, USA.

Brencich A, Sabia D (2008). Experimental identification of a multi-span masonry bridge: The Tanaro Bridge. *Construction and Building Materials*, 22(10), 2087-2099.

Brincker R, Zhang L, Andersen P (2000). Modal identification from ambient responses using frequency domain decomposition. *18th International Modal Analysis Conference*, San Antonio, USA, 625–630.

Çalık I, Bayraktar A, Türker T, Karadeniz H (2014). Structural dynamic identification of a damaged and restored masonry vault using ambient vibrations. *Measurement*, 55, 462–472.

Casciati S (2010). Response surface models to detect and localize distributed cracks in a complex continuum. *Journal of Engineering Mechanics*, 136(9), 1131–1142.

Deng L, Cai CS (2010). Bridge model updating using response surface method and genetic algoritm. *Journal of Bridge Engineering*, 15(5), 553-564.

Ewins DJ (1984). Modal Testing: Theory and Practice. Research Studies Press Ltd., England.

Foti D, Chorro SI, Sabba MF (2012). Dynamic investigation of an ancient masonry bell tower with Operational Modal Analysis - A non-destructive experimental technique to obtain the dynamic characteristics of a structure. *The Open Construction and Building Technology Journal*, 6, 384-391.

Friswell MI, Mottershead JE (1995). Finite Element Model Updating in Structural Dynamics. Kluwer Academic Publishers, Netherlands.

Gentile C, Saisi A, Cabboi A (2015). Structural identification of a masonry tower based on Operational Modal Analysis. *International Journal of Architectural Heritage*, 9(2), 98-110.

MacElroy DL, Kimpflen JF (1990). Insulation Materials, Testing and Applications. American Society for Testing and Material, USA.

Marcin L, Simone M, Bart P, Kim B, Peter B, Maciej K (2014). Updating finite element model of a wind turbine blade section using experimental modal analysis results. *Shock and Vibration*, 684786.

Nohutcu H, Demir A, Ercan E, Hokelekli E, Altintas G (2015). Investigation of a historic masonry structure by numerical and operational modal analyses. *The Structural Design of Tall and Special Buildings,* 24(13), 821–834.

Ren WX, Chen HB (2010). Finite element model updating in structural dynamics by using the response surface method. *Engineering Structures,* 32(8), 2455–2465.

Sevim B, Bayraktar A, Altunisik AC, Atamturktur S, Birinci F (2011). Finite element model calibration effects on the earthquake response of masonry arch bridges. *Finite Elements in Analysis and Design,* 47, 621-634.

SVS (2013). ARTeMIS Modal Pro 1.5. http://www.svibs.com

TSE 453 (2006). Turkish Standards Prefabricated Reinforced Components of Autoclaved Aerated Concrete. Ankara, Turkey.

Xin F, Shilin X, Xinong Z (2015). Model updating based on structural strain response using response surface method. *The 22nd International Congress on Sound and Vibration (ICSV22)*, Florence, Italy.

Zhouhong Z, Xiaoson L, Jie N (2015). Finite element model validation of bridge based on structural health monitoring Part I: Response surface-based finite element model updating. *Journal of Traffic and Transportation Engineering (English Edition),* 2(4), 258-278.

Challenge Journal of Structural Mechanics

The influence of elevated temperatures on the mechanical properties of polypropylene fiber reinforced concrete

Majid Atashafrazeh, Ahmet Ferhat Bingöl *, Murat Caf

Department of Civil Engineering, Atatürk University, 25240 Erzurum, Turkey

ABSTRACT

This paper describes the strength of Polypropylene Fiber Reinforced Concrete (PFRC) exposed to the elevated temperatures. In the study, control specimens without any fibers and the concrete specimens with the ratios of 0.30, 0.60, 0.90 and 1.20 kg/m^3 polypropylene fibers both in woolen and bar shape fiber have been produced. The specimens have been kept in the laboratory conditions for 28 days. Shortly after the curing period was completed, every group was heated at 23, 150, 300, 450, 600 and 750°C for two hours then the compressive strengths of them were determined. The maximum compressive strength was obtained by the specimens including 0.30 kg/m^3 woolen polypropylene. For this group, the compressive strength increase was 8% according to the control specimens. The compressive strengths of bar polypropylene fiber concrete were higher than the wool fibers under elevated temperatures. On the other hand, more compressive strength values are obtained from the control specimens than fiber groups at 600°C temperature. Melting the polypropylene fiber at 500°C formed some pore spaces in concrete and caused reduction of the compressive strength.

ARTICLE INFO

Article history:
Received 5 July 2017
Revised 25 July 2017
Accepted 6 August 2017

Keywords:
Polypropylene fiber reinforced concrete
Elevated temperature
Fiber type
Compressive strength

1. Introduction

In the field of civil engineering, the importance of fiber concrete is rapidly increasing. Polypropylene fiber reinforced concrete (PFRC) is the mixture of cement, aggregate, water and polypropylene fibers. Concrete undergoes significant damages when it is under the influence of elevated temperature. This may cause undesirable structural defects; however, addition of polypropylene fibers is one of the methods used to reduce this damage. According to the researches, the increase of plasticity and bending strength are the extra advantages of adding the fibers to the concrete. Two kinds of fiber that often used in the concrete are: steel fiber and polypropylene fiber (Kakooei et al., 2012; Mazaheripour et al., 2012). The evaporation of concrete surface water is a component in creating the contract paste fracture in concrete that leads to the formation of tension stress since the concrete starts to strengthen (Mazaheripour et al., 2012).

Recently, it has been found that fibers can also improve the residual properties of concrete being exposed to elevated temperatures. Polypropylene fibers have been used to reduce spalling and cracking and also to enhance the strength (Nishida and Yamazaki, 1995; Kalifa et al., 2001). But minimal or even negative effects of polypropylene fibers on the residual performance of the heated concrete were also observed (Chan et al., 2000; Poon et al., 2004). The fiber melts at approximately 160-170°C and causes expansion channels in the concrete. Therefore the additional porosity and small channels created by polypropylene fibers melting may lower internal vapor pressure in the concrete and reduce the likelihood of spalling (Noumowe, 2005; Uysal and Tanyıldızı, 2012). The loss in strength of concrete at high temperature was attributed to three major factors, namely vapor pressure of capillary and gel water, decomposition of cement hydration products, and possible collapse of filling aggregate (Haddad et al., 2008). Other researches have also shown that some organic fibers

* *Corresponding author*. Tel.: +90-442-2314770 ; E-mail address: afbingol@atauni.edu.tr (A. F. Bingöl)
ISSN: 2149-8024 / DOI: https://doi.org/10.20528/cjsmec.2017.08.013

such as polyvinyl alcohol (PVA) and nylon are also effective in mitigating spalling during the time that other materials like cellulose (Heo et al., 2009) and polyethylene fibers are not more effective (Knack, 2009; Bangi and Horiguchi, 2012).

The reductions in compressive strength of concrete, when exposed to elevated temperatures, can be attributed to the dehydration of concrete by driving out of free water and chemically combined water. The loss of physically bound water significantly affects the mechanical properties of the concrete exposed to elevated temperatures (Bastami et al., 2011). The fire resistance capacity of concrete is not complicated just because concrete is a composite material, in which components exhibit different thermal characteristics, but it is also for properties depending on the porosity and moisture of concrete. As the cement paste is exposed to increasing temperatures, the following process occurs: (1) the expulsion of steam water at a temperature of 100°C, (2) the beginning of the dehydration of the hydrates of calcium silicate at 180°C, (3) the decomposition of calcium hydroxide at a temperature of 500°C and (4) the decomposition of hydrate calcium silicate that begins around 700°C. The alterations produced by high temperatures are more evident when the temperature exceeds 500°C (Uysal et al., 2012; Khaliq and Kodur, 2011). Damage to the concrete exposed to elevated temperature includes weight loss, reductions in strength, modulus of elasticity and the formation of cracks and also large pores (Janotka and Mojumdar, 2005). In this study the strength of polypropylene concrete specimens exposed to the high temperature is achieved.

2. Experimental Program

2.1. Materials

2.1.1. Cement

The Portland cement CEM I 42.5 R has been used in this study. Initial and final setting times of the cement were 140 min and 205 min, respectively. The specific gravity of cement was 3.16 and the Blaine specific surface area was 3250 cm^2/g. Chemical composition of cement has been given in Table 1.

Table 1. Chemical composition of cement (%).

SiO_2	Al_2O_3	Fe_2O_3	CaO	MgO	SO_3	K_2O	Na_2O	Cl^-	Loss on Ignition
18.73	4.56	3.07	63.91	2.08	2.92	0.62	0.29	0.01	3.81

2.1.2. Woolen polypropylene (WPP) fiber

It is widely shown that polypropylene fibers are more affective in the concrete exposed to elevated temperatures (Suhaendi and Horiguchi, 2006; Bingöl and Atashafrazeh, 2015). Additives are used in polypropylene to prevent polymer degradation, resulting from exposure to heat, shear and light. Those additives broaden the property and application range by providing higher functionality and enhanced performance. As colorants, organic pigments provide solutions of high technical standard and are almost suitable for polyolefin. By polypropylene applications, the requirements for organic pigments expand and demand excellent processing properties as heat resistance or dispersibility and durable end-use properties as heat and weather fastness. Typical properties of polypropylene fiber (woolen type) have been shown in Table 2.

Table 2. Properties of woolen polypropylene fiber.

Fiber Type	BASF Master Fiber 15 MF
Length (mm)	12
Specific Gravity	0.91
Melt Point	160°C
Ignition Point	590°C
Shape	Woolen

2.1.3. Bar polypropylene (BPP) fiber

Addition of polypropylene fibers to concrete enhances the longevity of the structure by controlling micro cracks. Also, these fibers reduce water permeability, rebound "splattering" of concrete and shotcrete. Incorporating fibers increases concrete strength because of the high modulus of elasticity to compare with the concrete or mortar binder. Its post cracking behavior helps the continuity of absorbing energy as fibers pull out (Krishna et al., 2011). Typical properties of bar polypropylene fibers, used in this study, are given in Table 3.

Table 3. Properties of bar polypropylene fiber.

Fiber Type	Meyco Fiber SP 540
Length (mm)	40
Diameter (mm)	0.9
Fineness	44
Shape	Bar
Minimum Tension Strength (MPa)	295
Unit No. (fiber/kg)	4600

2.1.4. Aggregate

Thermal properties of concrete are mainly interrelated with the type of aggregates used in. Dry and clean natural, river aggregate was used in concrete mixture. The gravel was 16mm maximum nominal size with 1.1% water absorption value and relative density of it at saturated surface dry (SSD) condition was 2.70. The water

absorption value of the sand used was 1.2% and the relative density at saturated surface dry (SSD) condition was 2.61. The properties of aggregates used in this study have been given in Table 4.

2.2. Experimental significance

According to the ACI Committee 211 (2002) concrete is composed of aggregates, Portland cement, and water, and may contain other cementations' materials and chemical admixtures. The concrete mix that is used in this study for casting the specimens has been shown in Table 5. Portland cement CEM I 42.5 R, crushed stone course aggregates the maximum size of 16mm and river sand have been used. The specimens incorporated two different aspect fibers.

There were 9 different groups of the concrete specimens that consist of 0.30, 0.60, 0.90 and 1.20 kg/m^3 polypropylene fibers group both in woolen and bar types and also control group without any fibers admixtures. In this study totally 162 cylindrical concrete specimens were cast with the size of 200x100 mm. The specimens have been divided into six groups and exposed to six different (23, 150, 300, 450, 600 and 750°C) temperatures for 2 hours. The investigated parameters are chosen in accordance with the previous studies (Netinger et al., 2011; Gao et al., 2012; Aslani and Samali, 2012).

Table 4. The results of aggregates tests.

Grain Size (mm)	Sieve Size (mm)							Fineness Modulus	Specific Gravity	Loose Unit Weight (kg/m^3)	Unit Weight (kg/m^3)	Water abs. Ratio 24h (%)
	16	8	4	2	1	0.5	0.2					
0 - 4	100	100	86	62	39	16	4	2.66	2390	1288	1420	2.04
4 -16	100	31	8	1	0	0	0	5.9	2510	1310	1470	0.35

Table 5. Concrete mix proportion.

Water/Cement Ratio	Sand/Cement Ratio	Coarse Aggregate/Cement Ratio
0.46	2.66	2.45

3. Results and Discussion

3.1. Workability

Slump test is a common, convenient and inexpensive test, but it may not be a good indicator of workability for FRC (Song et al., 2005). However, once it has been established that a particular FRC mixture has satisfactory handling and placing characteristics at a given slump, the slump test may be used as a quality control test to monitor the FRC consistency from batch to batch according to the ACI committee 544 (1988). Fresh mixes were tested for workability by slump test. Slump test has been carried out for all the groups and test results are given in Table 6.

Table 6. Concrete specimens slump test result.

Concrete Group	Slump Result (cm)
Control	17
0.30 kg B.P.P. Fiber	16
0.60 kg B.P.P. Fiber	18
0.90 kg B.P.P. Fiber	19
1.20 kg B.P.P. Fiber	16
0.30 kg W.P.P. Fiber	13
0.60 kg W.P.P. Fiber	11
0.90 kg W.P.P. Fiber	11
1.20 kg W.P.P. Fiber	10

As the woolen polypropylene fiber amount increases in the concrete, the slump result comes down but increasing the bar polypropylene fiber does not have a significant influence on the slump results.

3.2. Weight loss

In this research concrete specimens (150 specimens) have been weighed before and after being exposed to the elevated temperatures. Weight loss percentages of them have been presented in Figs. 1 and 2 for bar and woolen polypropylene fibers, respectively.

It can be clearly seen that weight loss percentages of woolen polypropylene fiber concrete are more than the other one. It can also be seen in Fig. 1, for the bar polypropylene fiber concretes, minimum weight loss was observed in the group with 0.60 kg/m^3 fiber, when the maximum value was at 0.90 kg/m^3.

Fig. 2 shows weight loss of different groups of woolen polypropylene concrete in comparison with control group of specimens. It can be clearly seen that the group with 0.30 kg/m^3 woolen polypropylene has the minimum weight loss and maximum weight loss is observed for the group with 1.20 kg/m^3 woolen polypropylene fiber. Many potential causes of weight loss occur in the concrete being exposed to the high temperature (Bingöl and Atashafrazeh, 2015). However, expulsions of chunks or spalling of the concrete on the surface layers are main reasons of weight loss (Uysal et al., 2012).

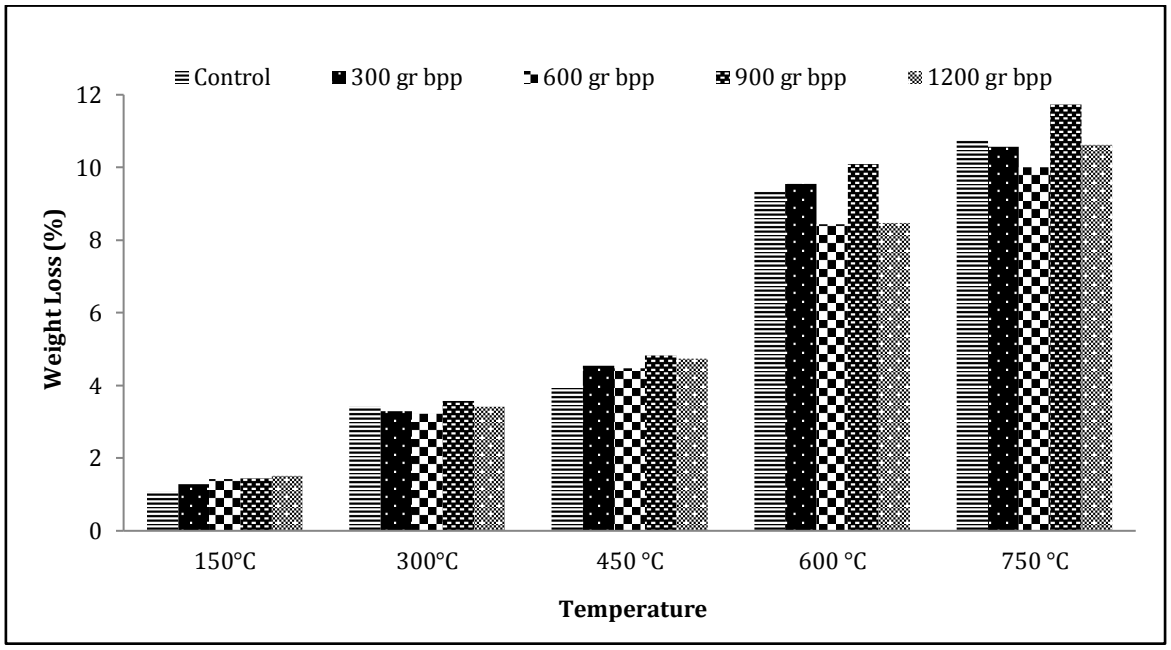

Fig. 1. Weight loss of bar polypropylene concrete in comparison with control concrete in different temperatures.

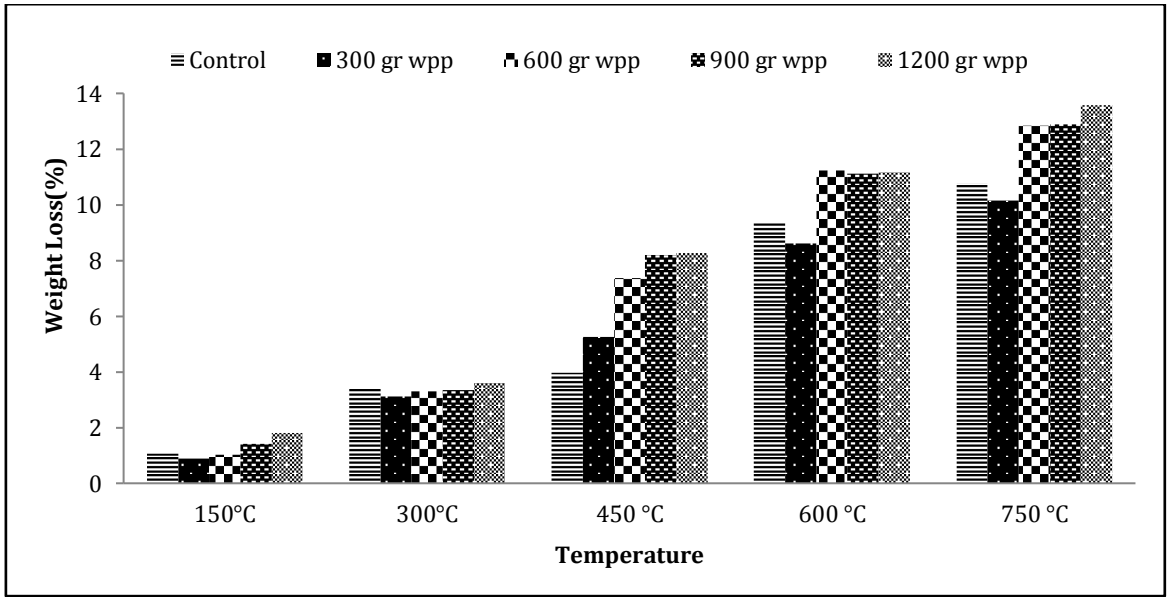

Fig. 2. Weight loss of woolen polypropylene concrete in comparison with control concrete in different temperatures.

3.3. Compressive strength

ASTM compressive strength equipment and procedures used for conventional concrete can also be applied for FRC. The cylinders should be 100x200 mm in size and should be made using external vibration or a 1 inch (25 mm) nominal width internal vibrator in accordance with ACI committee 544 (1988). Compressive performance of concrete at high temperature is important for the evaluation and repair of concrete structures (Zheng et al., 2012). The 28 days average compressive strength of specimens (totally 162 specimens) that were exposed to their specific elevated temperature has been shown in Table 7.

According to Table 7, it can be clearly seen that by the increase of the temperature, the compressive strength of specimens' decreased except at 450°C. Maximum compressive strength obtained for the specimens with 0.30 kg/m^3 woolen polypropylene fibers at 23°C. As it can be seen from the table, adding polypropylene fibers did not cause any significant increase in the compressive strength at room temperature (Behnood and Ghandehar M, 2009; Aulia, 2002). Maximum compressive strength for the concrete with 0.60 kg/m^3 bar polypropylene fiber was obtained at 150°C. It has been shown in the previous studies (Poon et al., 2004; Bastami et al., 2011) that heating up to temperature of 200°C does not have significant effects on the compressive strength of concretes. Maximum compressive strength values have been obtained for the concrete with 1.20 kg/m^3 bar polypropylene fiber at 300°C, for the concrete with 0.60 kg/m^3 bar polypropylene fiber at 450°C, for the control specimens at 600°C

and finally for the concrete with 1.20 kg/m^3 bar polypropylene fiber at 750°C. But it is significantly observed that, at 450°C the fibers had no influence on the compressive strength of concrete (Poon et al., 2004; Qian and Stroeven, 2000; Morris et al., 2002). The lower compressive strength of the concrete prepared with the polypropylene fibers may be because of the insufficient dispersing of the fibers in the concrete during mixing (Xiao and Falkner, 2006). The reduction in the compressive strength of concrete was significantly large for the specimens exposed to the high temperatures more than 600°C (Demirel and Keleştemur, 2010).

Table 7. Fibrous concrete mixes, average compressive strength after exposing to the elevated temperature (MPa).

Fiber Volume Fraction	23°C	150°C	300°C	450°C	600°C	750°C
Control	27.74	25.66	19.97	20.80	16.25	5.27
0.30 kg B.P.P Fiber	27.39	24.89	19.69	22.74	16.16	5.05
0.60 kg B.P.P Fiber	24.73	27.16	21.72	23.44	14.89	5.31
0.90 kg B.P.P Fiber	26.93	26.89	22.75	21.42	13.70	4.77
1.20 kg B.P.P Fiber	27.14	26.30	23.24	21.73	13.95	5.74
0.30 kg W.P.P Fiber	28.97	23.92	19.08	15.04	10.11	5.69
0.60 kg W.P.P Fiber	27.88	25.51	22.09	12.17	8.20	5.49
0.90 kg W.P.P Fiber	23.04	22.50	16.98	19.15	8.95	4.79
1.20 kg W.P.P Fiber	24.53	26.97	16.70	13.32	8.53	4.73

Compressive strength of concrete specimens exposed to the elevated temperatures has been shown in Figs. 3 and 4, which are represented by $y=ax+b$ indicated by the linear trend lines. R^2 is the coefficient of determination to evaluate simulation result. The value of R^2 varies between 0 and 1, where 1 is the perfect fit of the equation to underlying data (Zheng et al., 2012; Khaliq and Kodur, 2011).

All the specimens are compared with control specimens. Therefore, two figures have been shown, according to the figures, R^2 of control specimens is 0.8705. This value for 0.30, 0.60, 0.90 and 1.20 kg/m^3 bar polypropylene concrete specimens were 0.8076, 0.8349, 0.8775 and 0.8811 and for 0.30, 0.60, 0.90 and 1.20 kg/m^3 woolen polypropylene specimens are 0.9992, 0.9592, 0.8648 and 0.9268, respectively. These values showed a significant relationship among the results of the specimens.

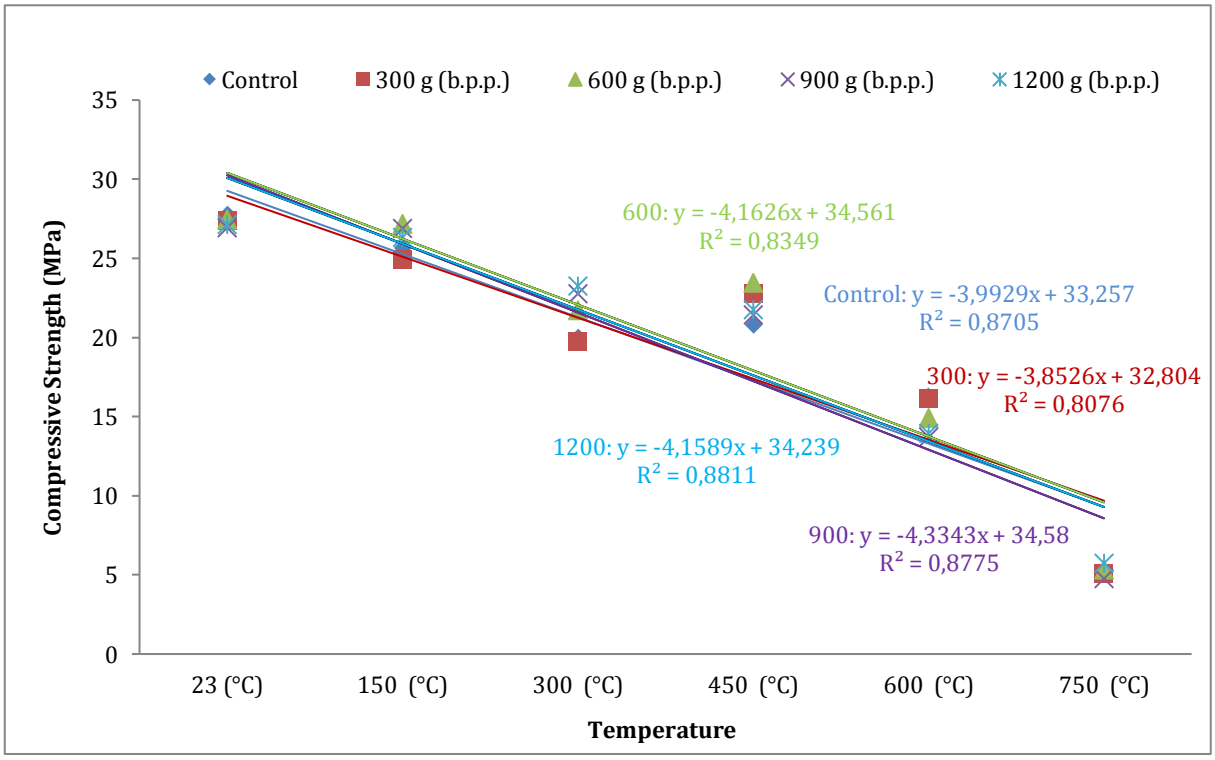

Fig. 3. Compressive strength of control and bar polypropylene fiber concrete.

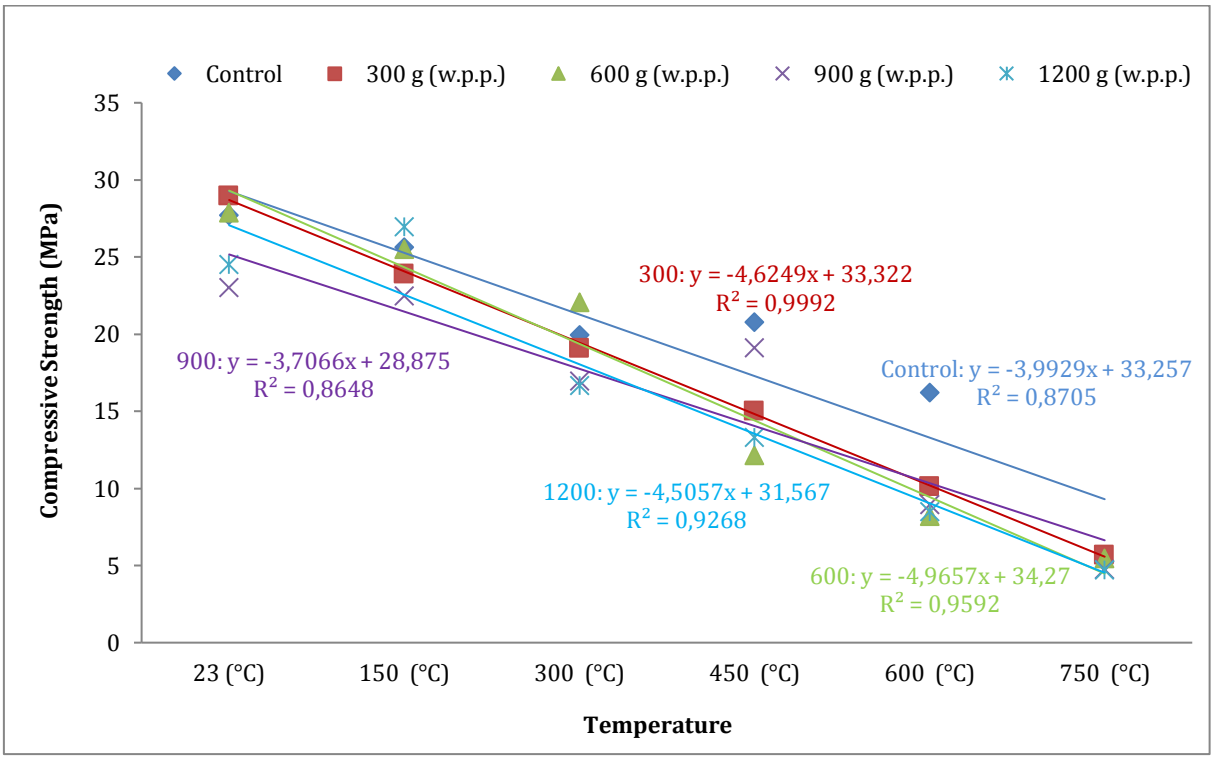

Fig. 4. Compressive strength of control and woolen polypropylene fiber concrete.

4. Conclusions

The main purpose of this study is investigating the effects of high temperature on the compressive strength of concrete. Therefore, the experiments were carried out by mixing woolen and bar types of polypropylene fiber into the concrete. The results obtained advantages compared to current knowledge and further specify with insertion.

- Less influence on the workability of bar polypropylene fibers on concrete has been determined. Therefore, the use of bar polypropylene fiber is thought to be appropriate in the pumped concretes. But woolen polypropylene fiber affects the workability of the fresh concrete adversely and it reduces the slump result almost 31% in comparison with control specimens' result.
- Polypropylene fiber has less influence on the compressive strength of concrete, and on the other hand, mixing in 1.20 kg/m^3 polypropylene fiber was being observed as a negative influence on them.
- In the compressive strength test, the maximum strength has been obtained for the concrete by mixing in 0.30 kg/m^3 woolen polypropylene fiber. The strength increase is about 8% in comparison with the control specimens.
- Bar polypropylene fiber is more effective than woolen type after being exposed to the elevated temperatures.
- In the specimens by mixing in 0.60 kg/m^3 bar polypropylene fiber, the highest strength has been obtained at 150°C (27.16 MPa). This result was 23.24 MPa for the specimens by mixing in 1.20 kg/m^3 bar polypropylene fiber at 300°C. And at 450°C, the maximum strength was 23.44 MPa for the concrete by the 0.60 kg/m^3 bar polypropylene fiber and finally control specimens gave the best results both at 600 and 750°C.
- The statistics show that the specimens without any fibers (control group) give the best results at 600°C. In the PFRC specimens, polypropylene fibers melt at 160-170°C and by increasing the temperature they vapor at 500°C, as well as preventing explosion of concrete, they can also influence the concrete to be a porous material. Therefore it leads to PFRC strength decreasing more than the control specimens.

References

ACI 211 (2002). Standard Practice for Selecting Proportions for Normal, Heavyweight, and Mass Concrete. American Concrete Institute, Michigan, ABD.

ACI 544 (1988). Measurement of Properties of Fiber-reinforced Concrete. American Concrete Institute, Michigan, ABD.

Aslani F, Samali B (2012). High Strength Polypropylene Fibre Reinforcement Concrete at High Temperature. School of Civil and Environmental Engineering, University of Technology, Sydney, Australia, Fire Technology.

Aulia TB (2002). Effects of polypropylene fibers on the properties of high strength concretes. *Lacer*, 7, 43-59.

Bangi MR, Horiguchi T (2012). Effect of fiber type and geometry on maximum pore pressures in fiber-reinforced high strength concrete at elevated temperatures. *Cement and Concrete Research*, 42, 459–466.

Bastami M, Khiabani A, Baghbadrani M, Kordi M (2011). Performance of high strength concretes at elevated temperatures. *Scientia Iranica, A*, 18(5), 1028–1036.

Behnood A, Ghandehar M (2009). Comparison of compressive and splitting tensile strength of high-strength concrete with and without polypropylene fibers heated to high temperatures. *Fire Safety Journal*, 44, 1015–1022.

Bingöl AF, Atashafrazeh M (2015). Compressive strength of polypropylene fiber concrete under the effects of high temperatures. *International Journal of Modern Manufacturing Technologies*, 7(1), 7-11.

Chan YN, Luo X, Sun W (2000). Compressive strength and pore structure of high-performance concrete after exposure to high temperature up to 800°C. *Cement and Concrete Research*, 30, 247–251.

Demirel B, Keleştemur O (2010). Effect of elevated temperature on the mechanical properties of concrete produced with finely ground pumice and silica fume. *Fire Safety Journal*, 45, 385–391.

Gao D, Yan D, Li X (2012). Splitting Strength of GGBFS concrete incorporating with steel fiber and polypropylene fiber after exposure to elevated temperatures. *Fire Safety Journal*, 54, 67–73.

Haddad RH, Al-Saleh RJ, Al-Akhras NM (2008). Effect of elevated temperature on bond between steel reinforcement and fiber reinforced concrete. *Fire Safety Journal*, 43, 334–343.

Heo YS, Sanjayan JG, Han CG, Han MC (2009). Effect of fiber type, length and numbers of fibers per unit volume on spalling protection of high strength concrete. *1st International Workshop on Concrete Spalling due to Fire Exposure*, Leipzig, Germany, 211–220.

Janotka I, Mojumdar SC (2005). Thermal analysis at the evaluation of concrete damage by high temperatures. *Journal of Thermal Analysis and Calorimetry*, 81(1), 197–203.

Kakooei S, Akil H, Jamshidi M, Rouhi J (2012). The effects of polypropylene fibers on the properties of reinforced concrete structures. *Construction and Building Materials*, 27, 73–77.

Kalifa P, Chene G, Galle C (2001). High-temperature behaviour of hpc with polypropylene fibers from spalling to microstructure. *Cement and Concrete Research*, 31, 1487–1499.

Khaliq W, Kodur V (2011). Thermal and mechanical properties of fiber reinforced high performance self-consolidating concrete at elevated temperatures. *Cement and Concrete Research*, 41, 1112–1122.

Knack I (2009). New Pp-fiber with exceptional melting characteristics for improved fire protection in concrete building. *1st International Workshop on Concrete Spalling Due to Fire Exposure*, Leipzig, Germany, 238–247.

Krishna Rao MV, Dakhshina Murthy NR, Kumar VS (2011). Behavior of polypropylene fiber reinforced fly ash concrete deep beams in flexure and shear. *Asian Journal of Civil Engineering*, 12(2), 143-154.

Mazaheripour H, Ghanbarpour S, Mirmoradi SH, Hosseinpour I (2011). The effect of polypropylene fibers on the properties of fresh and hardened lightweight self-compacting concrete. *Construction and Building Materials*, 25, 351–358.

Morris W, Vico A, Vazquez M (2002). Corrosion of reinforcing steel evaluated by means of concrete resistivity measurements. *Corrosion Science*, 44, 81–99.

Netinger I, Kesegic I, Guljas I (2011). The effect of high temperatures on the mechanical properties of concrete made with different types of aggregates. *Fire Safety Journal*, 46, 425–430.

Nili M, Afroughsabet V (2010). The effects of silica fume and polypropylene fibers on the impact resistance and mechanical properties of concrete. *Construction and Building Materials*, 24, 927–933.

Nishida A, Yamazaki N (1995). Study on the properties of high strength concrete with short polypropylene fiber for spalling resistance. *Proceedings of the International Conference on Concrete under Severe Conditions*, *CONSEC'95*, London, 1141– 1150.

Noumowe NA (2005). Mechanical properties and microstructure of high strength concrete containing polypropylene fibres exposed to temperatures up to 200°C. *Cement and Concrete Research*, 35, 2192–2198.

Poon CS, Shui ZH, Lam L (2004). Compressive behavior of fiber reinforced high-performance concrete subjected to elevated temperatures. *Cement and Concrete Research*, 34, 2215–2222.

Qian CX, Stroeven P (2000). Development of hybrid polypropylene-steel fibre-reinforced concrete. *Cement and Concrete Research*, 30, 63–69.

Song P, Hwang S, Sheu B (2005). Strength properties of nylon and polypropylene fiber reinforced concretes. *Cement and Concrete Research*, 35, 1546–1550.

Suhaendi SL, Horiguchi T (2006). Effect of short fibers on residual permeability and mechanical properties of hybrid fiber reinforced high strength concrete after heat exposition. *Cement and Concrete Research*, 36(9), 1672–1678.

Uysal M, Tanyıldızı H (2012). Estimation of compressive strength of self-compacting concrete containing polypropylene fiber and mineral additives exposed to high temperature using artificial neural network. *Construction and Building Materials*, 27, 404–414.

Uysal M, Yılmaz K, İpek M (2012). Properties and behavior of self-compacting concrete produced with GBFS and FA additives subjected to high temperatures. *Construction and Building Materials*, 28, 321–326.

Xiao J, Falkner H (2006). On residual strength of high-performance concrete with and without polypropylene fibers at elevated temperatures. *Fire Safety Journal*, 41(2), 115–121.

Zheng W, Li H, Wang Y (2012). Compressive behaviour of hybrid fiber-reinforced reactive powder concrete after high temperature. *Materials and Design*, 41, 403–409.

Challenge Journal of Structural Mechanics

Vertical stiffeners and internal pressure - influencing factors on distribution of meridional stresses in steel silos on discrete supports

Lyubomir A. Zdravkov *

Department of Metal, Wood and Plastic Structures, University of Architecture, Civil Engineering and Geodesy (UACEG), Sofia 1046, Bulgaria

ABSTRACT

Steel silos are interesting, complicated facilities. In order to ensure unloading of whole amount of stored product by gravity, they are often placed on supporting structure. Values of stresses in joints between thin sheets and supporting frame elements are very high, which could cause local loss of stability in thin shells. Many researchers have worked on values and distribution of the meridional stresses in that joints. Their traditional approach is to divide in their minds cylindrical shell on two parts - discretely supported ring beam and continuously supported shell above it. As a result of their efforts critical height of shell H_{cr} and ideal position of intermediate stiffening ring on shell are determined. The scientific results are based on semi-membrane theory of Vlasov, in which influence of vertical stiffeners and internal pressure is not accounted. On other hand all steel silos are loaded with an internal pressure and majority of them have vertical stiffeners above supports. Is it possible the obtained scientific results to be applied to these silos? In a present article the author will show that stiffeners and pressure should not be ignored in analysis.

ARTICLE INFO

Article history:
Received 20 June 2017
Revised 15 August 2017
Accepted 25 August 2017

Keywords:
Steel silo
Meridional stresses
Critical height
Vertical stiffeners
Internal pressure

1. Introduction

Often steel silos are elevated facilities, put on supporting structure. The purpose is easily and completely unloading of all stored product by gravity. The supporting structure is different for every project, depending on real conditions of exploitation. The most popular are two types - built from horizontal girders and columns or from columns only. Both types of frame structure cause concentrated meridional forces in the cylindrical body of the silo. As a result, the thin shell could loses local stability.

The simplest way to design steel silos is to divide in our minds cylindrical shell on two parts - discretely supported ring beam and continuously supported shell above it. Obviously, to ensure continuously support of shell, bending stiffness of ring beam should be high. In European standard EN 1993-4-1 that concept is recognized but it keeps silence about recommended stiffness of ring beam. Rotter (1985) suggested that a value of ratio ψ = 0,25 might be suitable for adoption in design, where:

$$\psi = \frac{K_{\text{shell}}}{K_{\text{ring}}}, \tag{1}$$

in which K_{shell} is stiffness of cylindrical shell; K_{ring} is stiffness of ring beam.

Based on English translation of differential equations of curved beam of Vlasov (1961), stiffness of ring beam K_{ring} is expressed as:

$$K_{\text{ring}} = \frac{(n^2-1)^2 EI_{\text{r}}}{R^4} \cdot \frac{1}{f_{\text{r}}}, \tag{2}$$

where n is number of uniformly spaced supports; E is modulus of elasticity; I_{r} is moment of inertia about a radial axis; R is radius of ring beam centroid.

$$f_{\text{r}} = 1 + \frac{EI_{\text{r}}}{n^2 K_{\text{T}}}, \tag{3}$$

* *Corresponding author*. Tel.: +359-885-081-305 ; E-mail address: zdravkov_fce@uacg.bg (L. A. Zdravkov)
ISSN: 2149-8024 / DOI: https://doi.org/10.20528/cjsmec.2017.08.014

in which:

$$K_{\mathrm{T}} = GJ + n^2 \frac{EC_{\mathrm{w}}}{R^2}, \tag{4}$$

where G is shear modulus; J is uniform torsion constant; C_{w} is warping constant for an open sections.

Semi-membrane theory of shells, proposed by Vlasov (1964), gives expression of stiffness of cylindrical shell, as following:

$$K_{\mathrm{shell}} = n\sqrt{\left(n^2 - 1\right)}\frac{E}{\sqrt[4]{3}}\left(\frac{t}{R}\right)^{3/2} \cdot \frac{1}{f_{\mathrm{s}}}, \tag{5}$$

where t is thickness of cylindrical shell.

$$f_{\mathrm{s}} = \frac{\left(e^{\eta}\right)^2 - 2 \cdot e^{\eta} \cdot \sin(\eta) - 1}{\left(e^{\eta}\right)^2 - 2 \cdot e^{\eta} \cdot \cos(\eta) + 1}, \tag{6}$$

in which:

$$\eta = \frac{2\pi H}{\mu}, \tag{7}$$

where H is height of cylindrical shell; μ is expressed by Calladine (1983) long wave bending half-wavelength:

$$\mu = \frac{2\pi\sqrt[4]{3}}{n\sqrt{(n^2 - 1)}}\sqrt{\frac{R}{t}}R. \tag{8}$$

Based on Eqs. (2) and (5), stiffness ratio ψ will look like as:

$$\psi = \frac{K_{\mathrm{shell}}}{K_{\mathrm{ring}}} = \frac{0.76(Rt)^2}{I_{\mathrm{r}}}\sqrt{\frac{R}{t}}\sqrt{\frac{n^2}{(n^2 - 1)^3}} \cdot \frac{f_{\mathrm{r}}}{f_{\mathrm{s}}}. \tag{9}$$

For simplification, Eq. (6) could be represented by two simple relations:

$$f_{\mathrm{s}} = \begin{cases} \dfrac{\eta}{3}, \text{when } H \le H_{\mathrm{cr}} \\ 1.0, \text{when } H > H_{\mathrm{cr}} \end{cases}, \tag{10}$$

where H_{cr} is critical height of cylindrical shell. It could be determined by formulae:

$$H_{\mathrm{cr}} = \frac{3\sqrt[4]{3}}{n\sqrt{\left(n^2 - 1\right)}}\sqrt{\frac{R}{t}} \cdot R. \tag{11}$$

H_{cr} represents height of shell which is effective of redistributing of discrete forces from supports. When height of shell $H \le H_{\mathrm{cr}}$, entire shell resists axial loads from supports. When $H > H_{\mathrm{cr}}$, only that part between bottom of shell and critical height H_{cr} is effective in redistributing of vertical reactions from discrete supports.

In his research of Topkaya and Rotter (2011a; 2011b) conducted extensive finite element analyses for verification of Rotter's criterion about stiffness of ring beam. With 1280 separate finite-element analyses (FEA), covering two different types of ring sections, various heights and radii of cylindrical shells, the authors checked validity of suggested by Rotter (1985) ratio ψ = 0,25. On basis of done FEA they concluded, when a stiffness ratio ψ ≤ 0.1, axial stresses will not deviate more than 25 % from the uniform support assumption.

Later Topkaya and Rotter (2014) determined ideal location of intermediate stiffening rings on the shell. They expect a ring, placed at this ideal position, can effectively remove all circumferential non-uniformity in the axial membrane stress above it. The simple expression of ideal height H_{I} is:

$$H_{\mathrm{I}} = \sqrt{12(1 + \nu)}\frac{R}{n}, \tag{12}$$

where ν is Poisson's ratio.

Eq. (12) is verified by the authors using a total of 2400 finite element analyses.

Necessary stiffness of intermediate stiffening rings is determined by Zeybek et al. (2015). Stiffness ratio χ could be expressed as:

$$\chi = \frac{K_{\mathrm{shell}}}{K_{\mathrm{stiffener}}} = \frac{Rt\left(AR^2 + {I_{\mathrm{x}}}^2(n^2 - 1)\right)}{12\sqrt{3}(1 + \nu)^{1,5} \cdot AI_{\mathrm{x}}n(n^2 - 1)^2}, \tag{13}$$

where K_{shell} is circumferential stiffness of the shell; $K_{\mathrm{stiffener}}$ is circumferential stiffness of circular ring; A is cross sectional area of the stiffening ring; I_{x} is moment of inertia of the stiffening ring about vertical axis "x-x".

The results in the research of Zeybek et al. (2015) indicate that ratios below about $\chi < 0.2$ provide a satisfactorily uniform axial membrane stress distribution above the intermediate ring stiffener, so this limit is recommended for practical design.

Common practice in design of real steel structures is to put stiffeners in point of application of concentrated loads. In our case, stiffeners should be positioned above discrete supports, see Fig. 1.

Fig. 1. Stiffeners in discrete supports of shell.

Additionally, all steel silos are storage facilities, loaded by radial internal pressure due to stored product. This is inevitable.

In all quoted researches above, in all equations, in all numerical models, influence of stiffeners and internal

pressure is missing. Which means that all their formulas are correct for smooth shells, axially loaded only. What about the other silos?

The author will try to check whether presence of vertical stiffeners and internal pressure has a substantially influence on distribution of meridional stresses and critical height of shell.

2. Analysis

For the purpose of analysis, a real steel silo in service will be used. Its parameters are as follow:

a) capacity - $V = 110$ m^3;
b) diameter - $D = 3485$ mm;
c) height of cylindrical shell - $H_s = 10950$ mm;
d) five courses, with thickness - $t_{s,1} = 7$ mm, $t_{s,2} = 6$ mm, $t_{s,3} = t_{s,4} = t_{s,5} = 4$ mm;
e) thickness of conical hopper - $t_h = 5$ mm;
f) stored product - lime.

Hopper is jointed to shell above bottom of first course, i.e. silo has a skirt. Angle section L100x10 is welded on opposite side of joint, see Fig. 2. Researched models of steel silos have two heights of skirt h_{sk}:

a) $h_{sk} = 500$ mm for Silo 1, Silo 2, Silo 3, Silo 4, Silo 5 and Silo 6;
b) $h_{sk} = 860$ mm for Silo 7, Silo 8, Silo 9, Silo 10, Silo 11 and Silo 12.

The second used height $h_{sk} = 860$ mm corresponds with Eq. (12) about ideal location of intermediate stiffening rings:

$$H_1 = \sqrt{12(1+\nu)}\frac{R}{n} = \sqrt{12(1+0.3)}\frac{1742.5}{8} = 860\,\text{mm}$$

On the top of shell is put another angle L100x10.

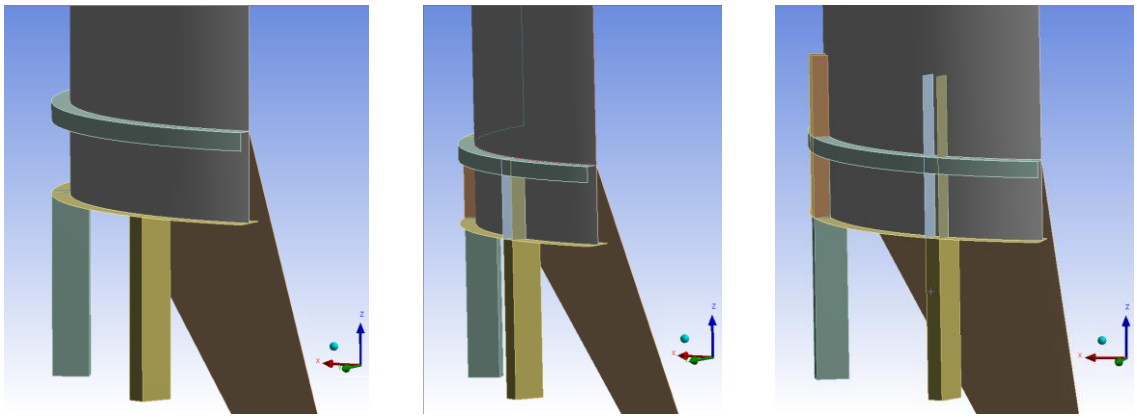

Silo 1 and Silo 7
no vertical stiffeners

Silo 2 and Silo 8
vertical stiffeners
with height 500 mm

Silo 3 and Silo 9
vertical stiffeners
with height 1000 mm

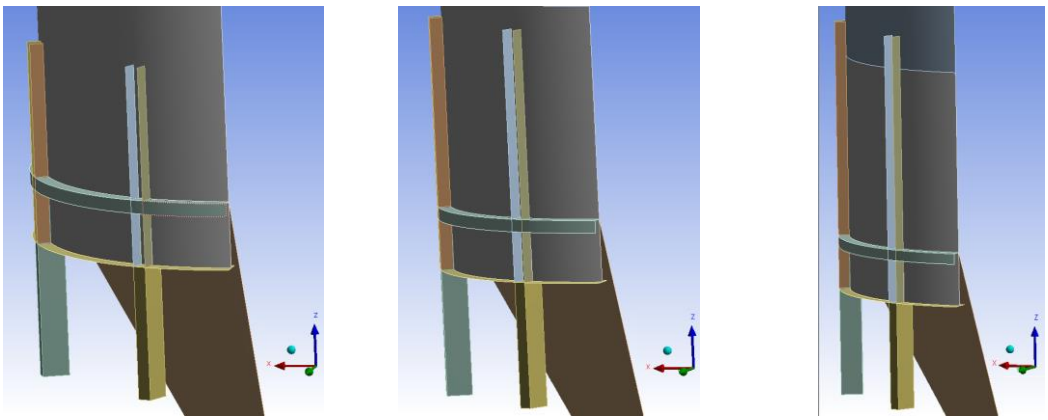

Silo 4 and Silo 10
vertical stiffeners
with height 1500 mm

Silo 5 and Silo 11
vertical stiffeners
with height 2000 mm

Silo 6 and Silo 12
vertical stiffeners
with height 2500 mm

Fig. 2. Vertical stiffeners on cylindrical shell.

No circular stiffener on top of the longer vertical stiffeners, see Fig. 2. No additional intermediate stiffening rings on the shell.

Under the skirt of silo are situated 8 columns with rectangular hollow section 200x100x8 mm. Bigger dimension of section is in radial direction, smaller - in circumferential. Height of all columns is 1000 mm. They are fixed to the ground (foundations). All elements are done by steel S235, with a properties according to European standard EN 10025-2:2004. First shell course, conical hopper and angle section L100x10 form stiffening ring as is shown on Fig. 3. It is accepted effective width of steel plates to be $16.t_i$ up and below the joint, according to standards API 650 and EN 14015.

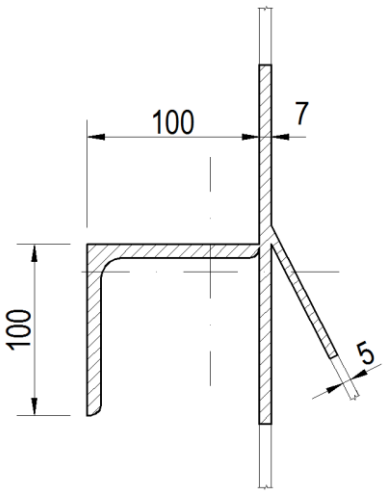

Fig. 3. Joint of hopper to cylindrical shell.

Geometrical characteristics of stiffening ring are:
a) area - A = 35.19 cm² ;
b) moment of inertia about vertical axis - I_x = 727.4 cm⁴.

Stiffness ratio χ according to Eq. (13) is:

$$\chi = \frac{Rt\left(AR^2 + I_x n^2 (n^2-1)\right)}{12\sqrt{3}(1+\nu)^{1,5}.AI_x n(n^2-1)^2}$$
$$= \frac{174{,}25 \cdot 0{,}7 \cdot \left(35{,}19 \cdot 174{,}25^2 + 727{,}4 \cdot 8^2 \cdot (8^2-1)\right)}{12 \cdot \sqrt{3} \cdot (1+0{,}3)^{1,5} \cdot 35{,}19 \cdot 727{,}4 \cdot 8 \cdot \left(8^2-1\right)^2}$$
$$= 0.0195$$

Accounted ratio χ = 0.0195 < 0.2, so stiffness should be enough for equal distribution of meridional stresses above the ring.

Using analytical software ANSYS are researched twelve models of silos, see Fig. 3. Differences between them are:
a) two heights of skirt h_{sk} , as is written above;
b) presence and height of vertical stiffening plates with section 8x100 mm.

For modelling of silos is used 2D element shell181. Quadrilateral method for meshing is used. Free face mesh method is "All quad". Max face size is 50 mm. Element's midside nodes are controlled by program.

ANSYS's option "symmetry" is activated to reduce a calculation time. In analysis is used a quarter of silo only.

Thin shell structures are sensitive for effect of changes of geometry during loading. On that reason geometrically nonlinear analyses (GNIA), described in EN 1993-1-6, were conducted.

On a first step, all silos are loaded by meridional (axial) force with value F = 800 kN, applied to upper edge of cylindrical shell as equal distributed load. The force F is applied on the top of shell to discover where meridional compressive stresses σ_x going to be equal to uniform meridional stresses $\sigma_{x,m}$. Where ratio reaches value $\sigma_x/\sigma_{x,m}$=1.0 is upper border of critical zone in shell, which redistributes vertical reactions from discrete supports.

On the second step, to meridional force F is added internal pressure as following:
a) on cylindrical shell - normal pressure p_n = 35 kPa;
b) on conical hopper:
- normal pressure - p_n = 35 kPa;
- tangential distributed load - p_t = 15,16 kPa.

Vertical force F and internal pressure are calculated for the real stored product (lime), according to standard EN 1991-4.

3. Results

In charts below, see Figs. 4 and 5, could be seen accounted by FEA change of ratio $\sigma_x/\sigma_{x,m}$ by height of shell, where: σ_x is meridional compressive stress by height of the cylinder; $\sigma_{x,m}=F/A$ is equal (uniform) meridional compressive stress, in which: F is the axial force, applied on the top of shell; A is the area section of cylindrical shell.

To ignore secondary stresses due to local effect of stiffening plates, meridional compressive stresses σ_x are measured in the middle between supports.

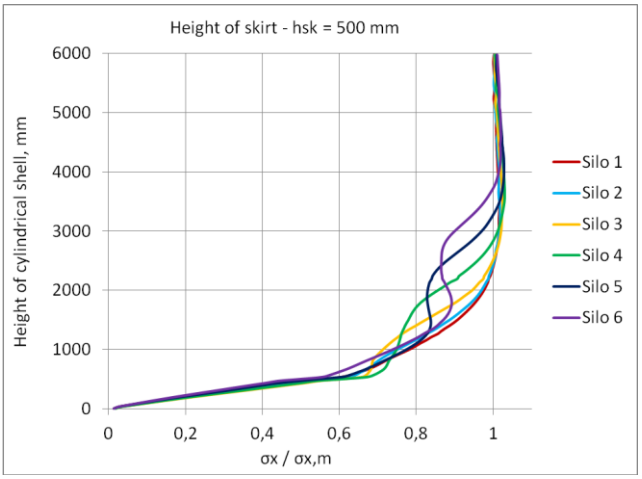

a) internal pressure is p = 0 (first step of loading)

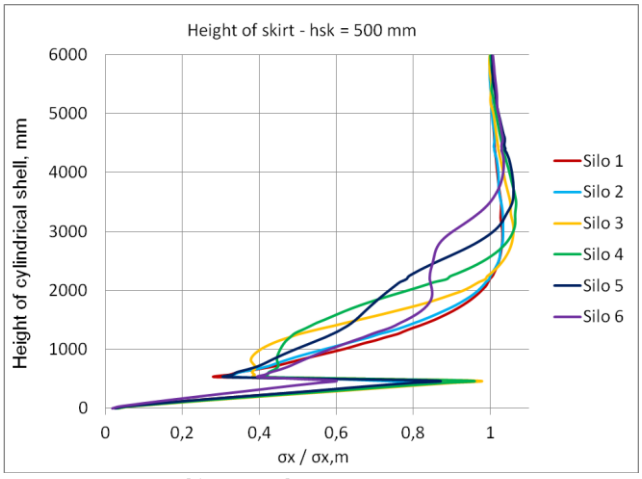

b) internal pressure is $p \neq 0$ (secondary step of loading)

Fig. 4. Change of ratio $\sigma_x/\sigma_{x,m}$ by height of shell (height of skirt h_{sk}=500 mm).

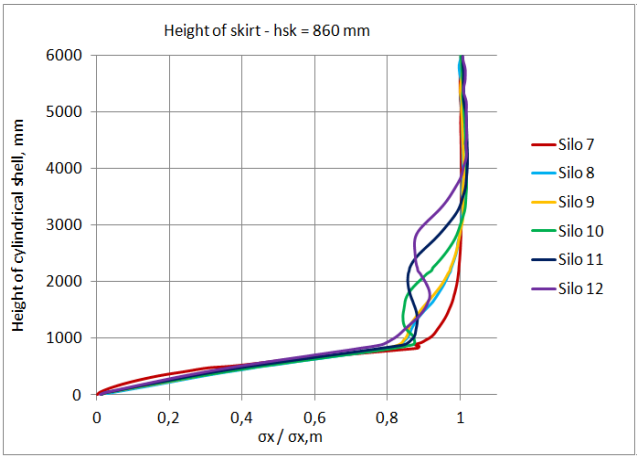

a) internal pressure is $p = 0$
(first step of loading)

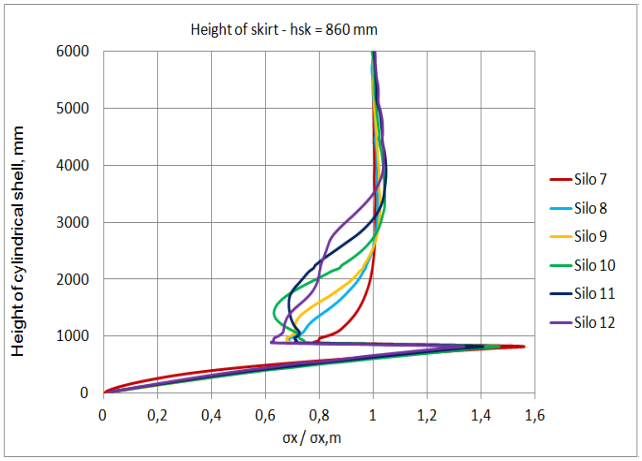

b) internal pressure is $p \neq 0$
(secondary step of loading)

Fig. 5. Change of ratio $\sigma_x/\sigma_{x,m}$ by height of shell (height of skirt h_{sk}=860 mm).

Value of critical height of shell H_{cr} should be calculated by Eq. (11):

$$H_{cr} = \frac{3\sqrt[4]{3}}{n\sqrt{(n^2-1)}}\sqrt{\left(\frac{R}{t}\right)}\cdot R$$

$$= \frac{3\sqrt[4]{3}}{8\sqrt{(8^2-1)}}\sqrt{\left(\frac{1742.5}{7}\right)}\cdot 1742.5 = 1709\,\text{mm}$$

Accounted by FEA lowest height, necessary to equalize values of σ_x and $\sigma_{x,m}$, refers to silos without vertical stiffeners. It is approximately H=2300 mm. Obviously it is higher than calculated by Eq. (11), but ratio $\sigma_x/\sigma_{x,m}$=0.94 on height H=1709 mm, i.e. difference is less than 25%.

Vertical stiffeners above supports increase critical zone in shell, which redistributes vertical reactions from discrete supports. For example, in silo 6 ratio $\sigma_x/\sigma_{x,m}$=1.0 on height H=3733 mm.

Internal pressure decreases with a little height of critical zone of shell. More important is its influence on change of forces/stresses below and above the joint with the hopper. In silos with high positioned hoppers, values of meridional normal stresses σ_x in skirt may exceed equal stress $\sigma_{x,m}$, see Fig. 5(b).

On Fig. 4 and Fig. 5 could be seen ratios $\sigma_x/\sigma_{x,m}$>1.0. It means that in part of the shell, meridional stresses in the middle, between supports, are bigger than meridional stresses above supports, see Fig. 6. A similar phenomenon has also been reported in a study of Knödel and Ummenhofer (2009).

Various height of skirt do not change critical height of shell. On other hand, placed on ideal position intermediate stiffening ring limits irregularity of meridional stresses above critical height.

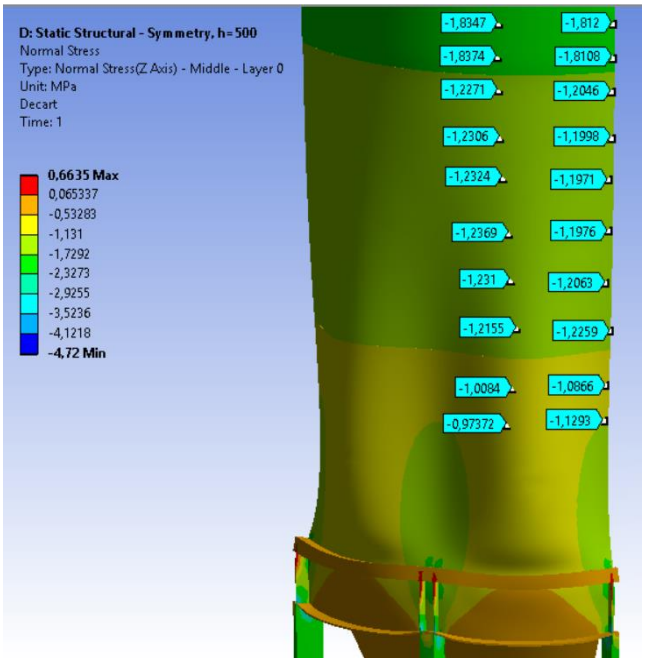

Fig. 6. Change of meridional normal stresses σ_x.

4. Conclusions

Real steel silos in service are loaded by radial internal pressure due to stored product. In addition, common practice in structural design is to put stiffeners in point of application of concentrated loads. In our case stiffeners should be positioned above discrete supports. In earliest researches about critical height of shell and ideal position of intermediate stiffening ring, influence of vertical stiffeners and internal pressure is not taken into account. In present article is verified whether they effect on height of critical zone in shell.

The main outcomes from the current research are:

- In space between bottom of first course and joint shell - hopper, presence or not of vertical stiffeners do not changes meridional stresses σ_x ;
- Vertical stiffeners, especially these with big length above horizontal joint silo - hopper, could change significantly ratio $\sigma_x/\sigma_{x,m}$;
- Presence of vertical stiffeners without stiffening ring on their top increase height of critical zone, which redistributes vertical reactions from discrete supports;
- Internal pressure, due to stored product, decreases with a little height of critical zone of shell. More important is its influence on change of stresses below and above the joint with the hopper;
- There are some parts of cylindrical shell, where meridional normal stresses above supports are smaller than these between supports.

REFERENCES

ANSYS, Release 17 (2016). ANSYS , Inc., Canonsburg, PA, USA.

API Standard 650 (2013). Welded Tanks for Oil Storage. Twelfth Edition. American Petroleum Institute, Washington, DC.

Calladine CR (1983). Theory of Shell Structures. Cambridge University Press, Cambridge, U.K.

EN 1991-4:2006 (2006). Eurocode 1 - Actions on structures - Part 4: Silos and tanks. European Committee for Standardization, Brussels.

EN 1993-1-6:2007 (2007). Design of steel structures - Part 1-6: Strength and Stability of Shell Structures. European Committee for Standardization, Brussels.

EN 1993-4-1:2007 (2007). Design of steel structures - Part 4-1: Silos. European Committee for Standardization, Brussels.

EN 10025-2:2004 (2004). Hot rolled products of structural steels - Part 2: Technical delivery conditions for non-alloy structural steels. European Committee for Standardization, Brussels.

EN 14015:2004 (2004). Specification for the Design and manufacture of site built, vertical, cylindrical, flat-bottomed, above ground, welded, steel tanks for the storage of liquids at ambient temperature and above. European Committee for Standardization, Brussels.

Knödel P, Ummenhofer T (2009). Silos with stepped wall thickness on local supports. *Proceedings of the International Association for Shell and Spatial Structures (IASS) Symposium*, Valencia.

Rotter JM (1985). Analysis and Design of Ringbeams. *In: Design of Steel Bins for Storage of Bulk Solids*, J. M. Rotter, ed., University of Sydney, Sydney, Australia, 164–183.

Topkaya C, Rotter JM (2011a). Ring beam stiffness criterion for column supported metal silos. *ASCE Journal of Engineering Mechanics*, 134, 846-853.

Topkaya C, Rotter JM (2011b). Stiffness of silo supporting ring beams resting on discrete supports. *6th International Conference on Thin-Walled Structures*, Timisoara, Romania.

Topkaya C, Rotter JM (2014). Ideal location of intermediate ring stiffeners on discretely supported cylindrical shells. *Journal of Engineering Mechanics*, 140(4), 04013001.

Vlasov VZ (1961). Thin-walled elastic beams. National Science Foundation, Washington, DC.

Vlasov VZ (1964). General theory of shells and its applications in engineering. NASA Technical Translation, TTF-99, Washington, DC.

Zeybek Ö, Topkaya C, Rotter JM (2015). Strength and stiffness requirements for intermediate ring stiffeners on discretely cylindrical shells. *Thin-Walled Structures*, 96, 64-74.

Challenge Journal of Structural Mechanics

Total potential energy minimization method in structural analysis considering material nonlinearity

Rasim Temür [a], Gebrail Bekdaş [a,*], Yusuf Cengiz Toklu [b]

[a] *Department of Civil Engineering, İstanbul University, 34320 İstanbul, Turkey*
[b] *Department of Civil Engineering, Okan University, 34959 İstanbul, Turkey*

ABSTRACT

Minimum potential energy principle is the basis of the most of the well-known traditional techniques used in the structural analysis. This principle determines the equilibrium conditions of systems with reference to minimization of the sum of the total potential energy of the structure. In traditional applications, this methodology is formulized by using matrix operations. A methodology has been proposed in the last decades for structural analyses based on the idea of using metaheuristic algorithms to obtain minimum potential energy of the structural system instead of following this classical approach. This new method, called "Total Potential Optimization using Metaheuristic Algorithms (TPO/MA)", has been applied in this paper to truss structures considering linear and nonlinear behavior of the structural material. The metaheuristic method used in this process is teaching-learning based optimization (TLBO) algorithm. The proposed technique is applied on numerical examples and results are compared with other techniques in order to test the efficiency of the proposed method. According to results obtained, TPO/MA method with TLBO algorithm is a feasible technique for the investigated problem.

ARTICLE INFO

Article history:
Received 25 December 2016
Accepted 25 February 2017

Keywords:
Teaching-learning based optimization
Total potential optimization
Metaheuristic algorithms
Nonlinear structural analysis
Truss

1. Introduction

According to minimum potential energy principle, a structural system is in equilibrium if the total potential (TP) of the system is minimum. Classical methods do apply this principle in its pure form only in solving some demonstrative problems. The usual practice starts by writing down the TP in matrix form, as $TP = x^T Ax - Px$ where *x* is the vector of displacements, P is the vector of acting loads, and A is the flexibility matrix of the system. This is then followed by taking the derivative of TP with respect to x, and equating it to zero in the form $Ax = P$. This latter step is actually the application of the minimum energy principle which aims at finding *x* making TP stationary. Then the matrix equation $Ax = P$ is solved by using anyone of the well-established methods of matrix inversion or solving systems of linear equations. The method described here is valid for linear systems. For nonlinear systems there does not exist a common technique. The solutions for such systems vary according to type of nonlinearity (material nonlinearity, large deflections, nonlinear supports, under-constrained structures, missing or failing members, unstable structures, etc.) and a technique applicable for one type of nonlinearity is not applicable for another type except in some very special cases.

The method described in this paper, on the other hand, is valid for all types of linear and nonlinear structures, whatever the type of nonlinearity is. This technique, called "Total Potential Optimization using Metaheuristic Algorithms (TPO/MA)" is made possible thanks to advances in computer technology as to speed and also to emergence of and advances in metaheuristic algorithms for optimization problems. In this method, metaheuristic algorithms are employed for finding the displacements in a structure that makes the TP of the system a minimum. TP of the system is written as the sum of exact TP's of parts of the system. In this way the

* *Corresponding author*. Tel.: +90-212-4737070 ; Fax: +90-212-4737180 ; E-mail address: bekdas@istanbul.edu.tr (G. Bekdaş)
ISSN: 2149-8024 / DOI: https://doi.org/10.20528/cjsmec.2017.02.005

formulation does not necessitate use of matrices so that no big computer memory capacities become needed. Until recently the TPO/MA has been applied to a wide variety of problems such as truss, cables and tensegrity structures (Toklu 2004; Toklu et al., 2013; Temür et al., 2014; Toklu et al., 2015; Toklu and Uzun, 2016) using different types of metaheuristic algorithms.

In this paper, TPO/MA method is employed for structural analyses of trusses with nonlinear material properties. The metaheuristic algorithm used is a recently developed one, namely the teaching-learning based optimization (TLBO) algorithm. In order to evaluate the performance of TLBO algorithm, results are compared with those mentioned in the existing literature.

2. Methodology

Metaheuristic algorithms are developed from mathematical identification of natural phenomena. For example, Genetic algorithm (GA) mimics the process of natural selection (Holland, 1975 and Goldberg, 1989), particle swarm optimization (PSO) is inspired from the social behavior of animals (Kennedy and Eberhart, 1995), ant colony optimization (ACO) imitates the behavior of ants seeking a path between their colony and a source of food (Dorigo et al., 1996), harmony search (HS) is conceptualized on musician performance for seeking a harmony to admire the people (Geem et al., 2001).

The teaching-learning based optimization (TLBO) (Rao et al., 2011) is developed based on inspiration of teaching and learning procedure in a classroom. The method is not based on specific parameters and this is the most remarkable part of it. This property makes TLBO easily applicable and versatile among other metaheuristic algorithms.

The optimization process of the TLBO algorithm can be explained under two titles, namely First calculations and Iteration.

***First Calculations*:** In the first calculations step, data of the structural system are defined. This data contains information about supports, start and end points of structural members, cross sectional areas of members, parameters about material properties of members, etc. In addition to the data, the upper and lower limits of the design variables, population number and maximum iteration number (as stopping criterion) are also defined in this section. Coordinates of the joints of the deformed system are the design variables of the problem.

Then, by randomizing the design variables between their defined limits, a group of the structures is obtained. This group is defined as initial solution matrix and number of structures (or solution vectors) in the group is equal to population size (*pn*). At the end of this step, the strain energy (Eq. (1)), work done by external loads (Eq. (2)) and total potential energy (Eq. (3)) for each generated system (or objective function) are calculated for future comparisons.

$$U = \frac{1}{2}\int_{VOLUME} \varepsilon^T \sigma dV \,, \tag{1}$$

$$W = \int_{S_1} \left(T_x u + T_y u + T_z u\right) dS \,, \tag{2}$$

$$\Pi = U - W = \frac{1}{2}\int_{VOLUME} \varepsilon^T \sigma dV - \int_{S_1} \left(T_x u + T_y u + T_z u\right) dS. \tag{3}$$

In Eqs. (1-3), ε^T is the strain vector, σ is the stress vector and V is the volume of the body, u, v, and w are displacements in the x, y, and z directions, and T_x, T_y and T_z are the components of external forces in x, y, and z directions. The objective function of the problem is to minimize the total potential energy of the system (Eq. (3)).

***Iterations*:** This process contains two phases: teacher (*tp*) and learner (*lp*) phases. In the teacher phase, new solution vectors are generated according to the best solution vector ($X_{teacher}$) which is the vector currently having the minimum value for TP of the system. Formulation of the generation of new values can be written as

$$X_{new,i}^{ip} = X_{old,i} + rnd(0,1) \cdot (X_{teacher} - T_F \cdot X_{mean}) \,, \tag{4}$$

where $X_{old,i}$ is previous values of the design variables, X_{mean} is the mean value of the design variables, *rnd* is a uniformly distributed random numbers within the range of [0, 1] and T_F is an integer number that takes a value 1 or 2 (Eq. (5)).

$$T_F = round[1 + rnd(0.1)] \rightarrow \{1 - 2\} \,. \tag{5}$$

In the learner phase, the value of new solution are generated from the two existing vectors that are randomly chosen from the solution matrix. The expression of the learner phase is defined as

$$X_{new,i}^{Ip} = \begin{cases} X_{old,i} + rnd \cdot \left(X_i - X_j\right); & f(X_i) > f(X_j) \\ X_{old,i} + rnd \cdot \left(X_j - X_i\right); & f(X_i) < f(X_j) \end{cases}, \tag{6}$$

in which $f(X_i)$ and $f(X_j)$ are objectives of selected vectors. After application of both phases, the objective functions of new vectors are calculated and if it is better than the old one, it is replaced with the old one. Iteration process is repeated until the maximum iteration number is satisfied. The optimization process is summarized in the pseudo code given in Fig. 1.

3. Numerical Examples

Numerical examples are presented in this section considering a 6-bar plane truss (Fig. 2) (Toklu, 2004) and three type of materials. In order to show the efficiency of the proposed method the results are compared with HS algorithm. The cross sectional areas of members 2-4 are 100 mm^2 and cross-sectional areas of other members are 200 mm^2. A concentrated load with 150 kN density is applied to system at joint 4. The first material considered (MAT 1) is a linear one with elasticity modulus of $2 \cdot 10^5$ N/mm^2. The second material (MAT 2) is a bilinear one, the third one (MAT 3) represents a highly nonlinear material. Stress-strain diagrams for all these materials are presented in Fig. 2(b).

```
Randomly generate the initial students
Calculate objective function
While stopping criteria
    (Teacher Phase)
    Calculate the mean of each design variable
    Identify the best student as teacher
    For i=1:N_variable
        Calculate teaching factor Eq. (5)
        Create a new solution based on teacher Eq. (4)
        Calculate objective functions for the new solutions Eq. (3)
        If X_new is better than X_old
            X_old = X_new
        End If
    End For
    (Learner Phase)
    For i=1:N_variable
        Select any two solution randomly [i, j]
        Create a new solution based on selected solutions Eq. (6)
        Calculate objective function for the new solution
        If X_new is better than X_old
            X_old = X_new
        End If
    End For
End While
```

Fig. 1. Pseudo code of optimization process with TLBO.

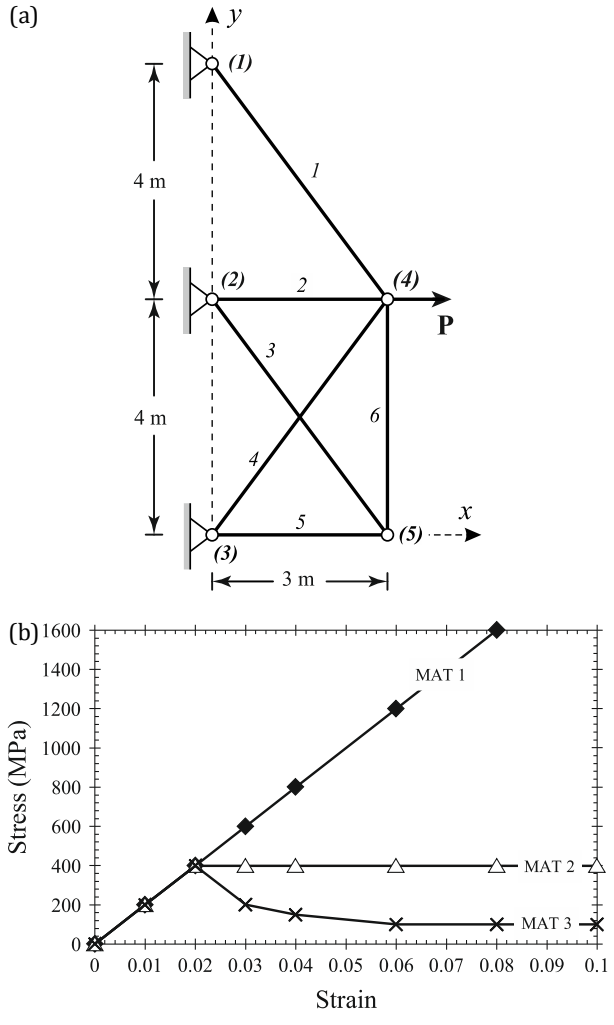

Fig. 2. (a) 6-bar plane system;
(b) Material properties of problem.

In Figs. 3-5, for all these three materials, plots about the convergence to optimum result of TLBO and HS is given where the population number is equal to 10. On the TLBO approach, optimum results are found after about 100, 400 and 800 cycles for MAT 1, MAT 2 and MAT 3, respectively. For the HS based analyses, these numbers are about 2500, 500000 and 500000, respectively. It can be concluded here that convergence for linear material is much better than other materials and, for all cases, convergence performance of TLBO is better than HS approach.

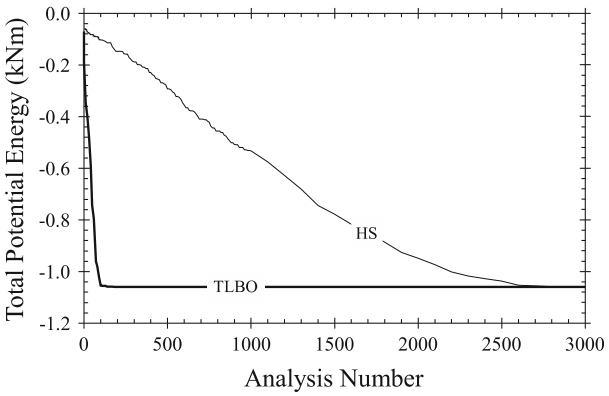

Fig. 3. Convergence to optimum results for MAT 1.

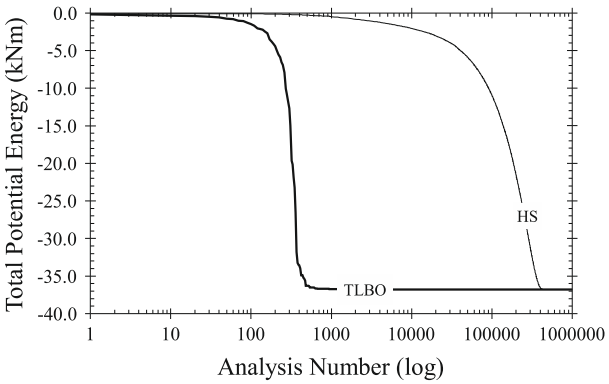

Fig. 4. Convergence to optimum results for MAT 2.

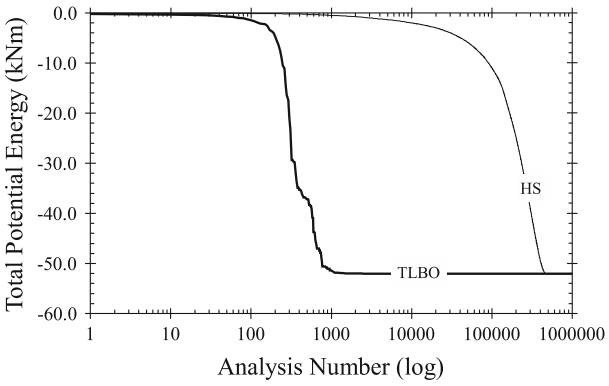

Fig. 5. Convergence to optimum results for MAT 3.

In order to investigate the effect of population number when applying TLBO on number of cycles, computations are repeated for seven different population numbers (Fig. 6). According to results, for all cases,

analyses numbers needed for obtaining optimum results increase almost linearly as the population number increases. Statistical treatment of results for different population number is summarized in Table 1. According to these tests, results are all acceptable except for population number as 5. For case where population number is 10 or greater, the difference between the upper and lower bounds obtained for minimum potential energy is negligible so that the standard deviations are very small.

Table 1. Optimum result for different population number.

		5V	*10V*	*15V*	*20V*	*25V*	*30V*	*35V*	*40V*
	Min	-1059735	-1059735	-1059735	-1059735	-1059735	-1059735	-1059735	-1059735
MAT1	*Max*	**-1035346**	-1059735	-1059735	-1059735	-1059735	-1059735	-1059735	-1059735
	St Dev	**3192.258**	0.024875	1.86×10^{-9}	1.86×10^{-9}	1.86×10^{-9}	1.86×10^{-9}	1.86×10^{-9}	1.86×10^{-9}
	Min	-3.68×10^{7}	-3.68×10^{7}	-3.68×10^{7}	-3.68×10^{7}	-3.68×10^{7}	-3.68×10^{7}	-3.68×10^{7}	-3.68×10^{7}
MAT2	*Max*	$\mathbf{-3.62\times10^{7}}$	-3.68×10^{7}	-3.68×10^{7}	-3.68×10^{7}	-3.68×10^{7}	-3.68×10^{7}	-3.68×10^{7}	-3.68×10^{7}
	St Dev	**55387.39**	0.011541	8.2×10^{-8}	8.2×10^{-8}	8.2×10^{-8}	8.2×10^{-8}	8.2×10^{-8}	8.2×10^{-8}
	Min	-5.21×10^{7}	-5.21×10^{7}	-5.21×10^{7}	-5.21×10^{7}	-5.21×10^{7}	-5.21×10^{7}	-5.21×10^{7}	-5.21×10^{7}
MAT3	*Max*	$\mathbf{-5.02\times10^{7}}$	-5.21×10^{7}	-5.21×10^{7}	-5.21×10^{7}	-5.21×10^{7}	-5.21×10^{7}	-5.21×10^{7}	-5.21×10^{7}
	St Dev	**186907.6**	0.001228	7.45×10^{-9}	7.45×10^{-9}	7.45×10^{-9}	7.45×10^{-9}	7.45×10^{-9}	7.45×10^{-9}

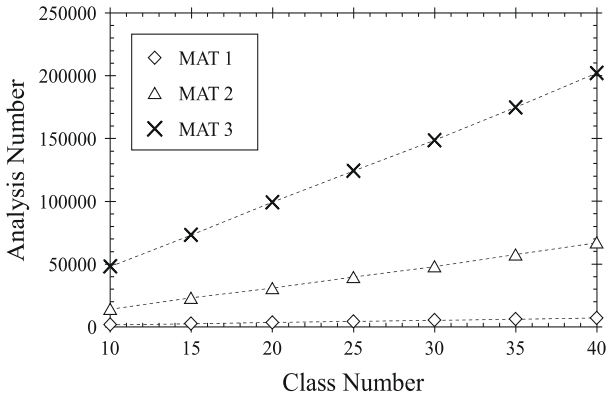

Fig. 6. Analysis number vs. population number plot.

In Figs. 7-9, total potential energy values for increased loading from 0 kN to 150 kN are given. The effects of material properties on total energy values can be clearly seen on the figures. The energy graph is quite monotonic for linear MAT 1 material, but sudden changes become observed for the other nonlinear materials MAT 2 and MAT 3.

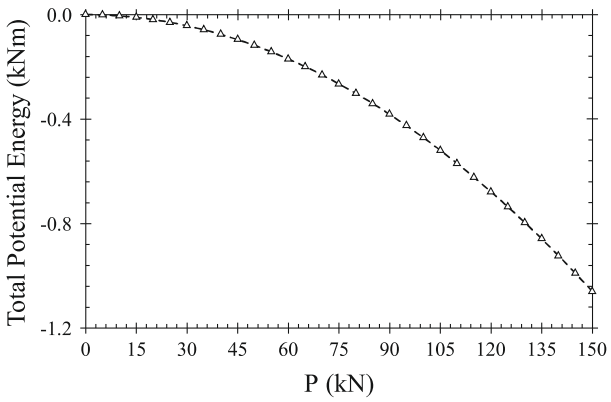

Fig. 7. Potential energy value of increasing loading for MAT1 material.

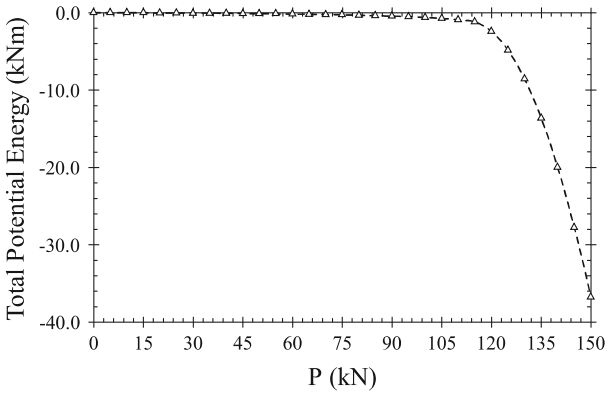

Fig. 8. Potential energy value of increasing loading for MAT2 material.

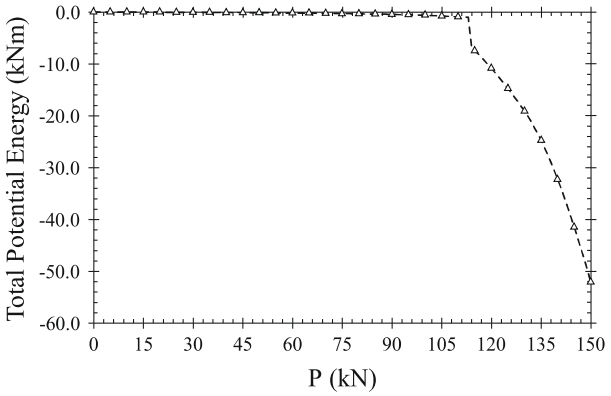

Fig. 9. Potential energy value of increasing loading for MAT3 material.

4. Conclusions

The analyses of truss systems are investigated by using TPO/MA method for different material properties such as linear, bilinear and nonlinear. The efficiency of the proposed TLBO method is checked by comparing

with results obtained by HS approach. According to results, both TLBO and HS algorithms gave the same minimum potential energy for all material cases. Comparing the computational times (analyses numbers for optimum results) of the methods, the TLBO approach is 20% to 80% shorter than HS algorithm. According to observation of the effect of population numbers on analyses number, if the population number of TLBO is equal to or more than 10, the minimum energy value can be successfully found. But comparing the statistical suitability and analyses number, using a population number defined as 10 can be the best selection.

REFERENCES

Dorigo M, Vittorio M, Alberto C (1996). Ant system: Optimization by a colony of cooperating agents. *Systems, Man, and Cybernetics, Part B: Cybernetics, IEEE Transactions*, 26.1, 29-41.

Geem ZW, Kim JH, Loganathan GV (2001). A new heuristic optimization algorithm: harmony search. *Simulation*, 76, 60-68.

Goldberg DE (1989). Genetic Algorithms in Search, Optimization and Machine Learning. Addison-Wesley Longman Publishing.

Holland JH (1975). Adaptation in Natural and Artificial Systems. University of Michigan Press.

Kennedy J, Eberhart RC (1995). Particle swarm optimization. *Proceedings IEEE International Conference on Neural Networks*, 4(1942), Perth, Australia.

Rao RV, Savsani VJ, Vakharia DP (2011). Teaching-learning-based optimization: a novel method for constrained mechanical design optimization problems. *Computer-Aided Design*, 43(3), 303-315.

Temur R, Bekdaş G, Toklu YC (2014). Analysis of cable structures through total potential optimization using meta-heuristic algorithms. In *ACE2014, 11th International Congress on Advances in Civil Engineering*, 21-25.

Toklu YC (2004). Nonlinear analysis of trusses through energy minimization. *Computers and Structures*, 82(20-21), 1581-1589.

Toklu YC, Temur R, Bekdas G, Uzun F (2013). Space applications of tensegric structures. *RAST 2013 - Proceedings of 6th International Conference on Recent Advances in Space Technologies*, 29-32.

Toklu YC, Temür R, Bekdaş G (2015). Computation of nonunique solutions for trusses undergoing large deflections. *International Journal of Computational Methods*, 12(03), 1550022.

Toklu YC, Uzun F (2016). Analysis of tensegric structures by total potential optimization using metaheuristic algorithms. *Journal of Aerospace Engineering*, 04016023.

Challenge Journal of Structural Mechanics

The strain sensitivity of brass fiber reinforced concrete

Egemen Teomete *, Erman Demircilioğlu, Serap Kahraman

Department of Civil Engineering, Dokuz Eylül University, 35160 İzmir, Turkey

ABSTRACT

The structures are challenged by earthquakes and other environmental factors. Structural health monitoring is crucial to protect the lives. The strain gages used in structural health monitoring have low durability and can get point wise measurements which limit their use. In this study, five different concrete mixtures with different brass fiber volume fractions were designed. Along with the control mixture which does not have brass fiber, six mixtures were designed and three cube samples from each mixture were cast and cured. Compression test was conducted with simultaneous measurement of electrical resistance. The brass fiber reinforced concrete has strong linear relationship between the electrical resistance change and strain. Important progress was achieved in development of "Smart Concrete" which can sense its strain and damage.

ARTICLE INFO

Article history:
Received 6 February 2017
Accepted 25 February 2017

Keywords:
Smart concrete
Self-sensing
Electrical resistance
Compression test
Smart structures
Brass fiber

1. Introduction

Earthquakes and other environmental factors degrade and damage civil structures. Concrete infrastructures, have materials deteriorations and 30% of the bridges were reported to be structurally not reliable in USA (Reza et al., 2003). Structural health monitoring is vital to protect the people and structures. Commercial metal foil strain gauges measures the strain of a point and they have low durability and short life time. Moreover, many strain gauges have to be used to monitor structure health which increases cost (Chung, 2001). This study is a contribution of developing self-sensing smart materials and structures for the construction industry.

Piezoresistive effect is the change of electrical resistance under application of load (Chung, 1998; Fu et al., 1997). Cementitious materials were tested with two and four electrode methods for electrical resistance. Current application and the voltage measurement were carried out with the same pair of electrodes in the two electrode method while different electrode pairs were used in the four electrode method (Han et al., 2007; Chiarello and Zinno, 2005). Embedded and circumferential electrode methods were used. In circumferential electrode method, conductive band or dyestuffs were stuck around samples. In embedded electrode method, conductive mesh, wire or plate were sink into samples (Chen and Liu, 2008; Teomete and Erdem, 2011; Li et al., 2008; Li et al., 2006).

Tensile strain sensitivity of cementitious composites was tested by split tensile test and high strain sensitivity was obtained (Teomete and Koçyiğit, 2013). There is strong linear relationship between crack length and electrical resistance change of cement composites (Teomete, 2013). Transverse strain sensitivity of cement matrix composites was tested by compression and split tensile tests (Teomete, 2014).

2. Material and Experimental Method

Six different mixes were designed in this study (M0, Br1, Br2, Br3, Br4, Br5). CEM II B-M (L-W) 42,5R cement were used in all mixes. All mixes were prepared according to TS 802 "Design of Concrete Mixes". Water /binder ratio 0.37; silica fume/binder ratio 10%, super-plasticizer/binder ratio 1% was used in all mixes. Commercially available brass fiber which had average length of 1.5 mm and average diameter of 0.5 mm was used in mixes M0, Br1, Br2, Br3, Br4 and Br5 at 0, 0.35, 0.5, 0.8, 1, 1.5% volumetric ratios, respectively. In M0, there is

* *Corresponding author*. Tel.: +90-232-3017060 ; Fax: +90-232-4531192 ; E-mail address: egemen.teomete@deu.edu.tr (E. Teomete)
ISSN: 2149-8024 / DOI: https://doi.org/10.20528/cjsmec.2017.02.008

not any brass fiber. Super plasticizer was modified polycarboxylates based polymer (ViscoCrete High Tech 30). Aggregates 0-5 mm and 5-15 mm were used according to TS802 grading limits.

7.5 cm cube molds were used for casting samples. The molds have four slots which were 2 mm wide and 55 mm long, on each side. Pure copper wire mesh which has hole size 5 mm, wire diameters 0.6 mm were used as electrodes and placed into molds (Fig. 1(a)). The mix was cast in the mold as in Fig. 1(b). The samples were taken out of molds 24 hours after casting, and cured in water for 28 days.

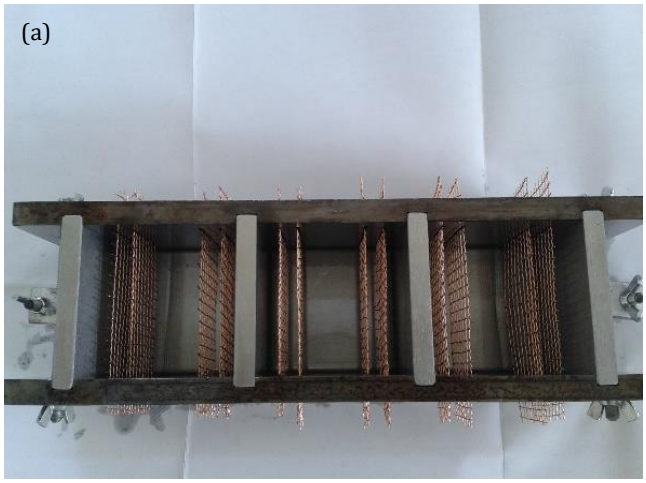

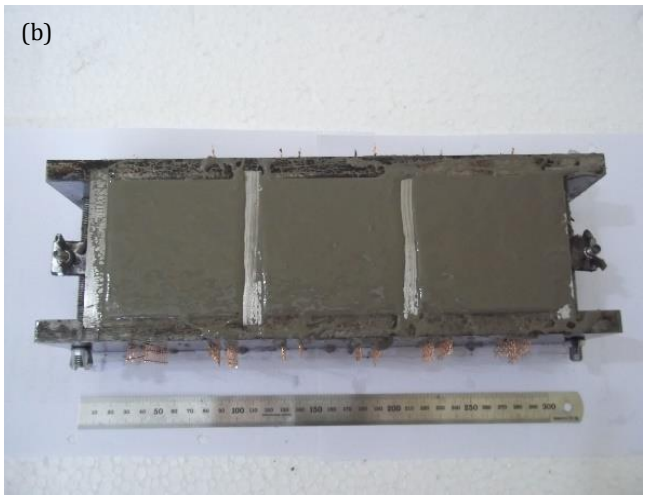

Fig. 1. (a) Mold and electrodes; (b) After casting.

Compression test was applied in order to investigate the relations between compressive strain and electrical resistance change as in Fig. 2. Shimadzu mechanical testing machine was used for the tests with a load rate of 0.5 mm/min. During the test, DC 20 V was supplied to outer two electrodes while potential difference between inner electrodes were measured as V_s (Fig. 2(a)). The reference resistance R_r=1000 Ohms was used and its voltage was recorded was V_r. The current in the circuit was measured as I_c. Voltages, V_s and V_r, current I_c, sample strain, load were recorded at a rate of 10 Hz during the test (Figs. 2(a, b)). Glass fiber epoxy composites were used to isolate the sample from steel plates during the test.

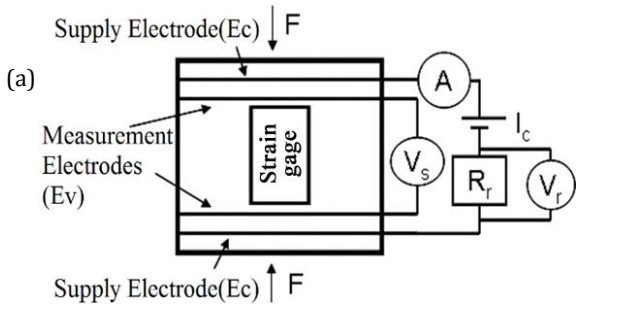

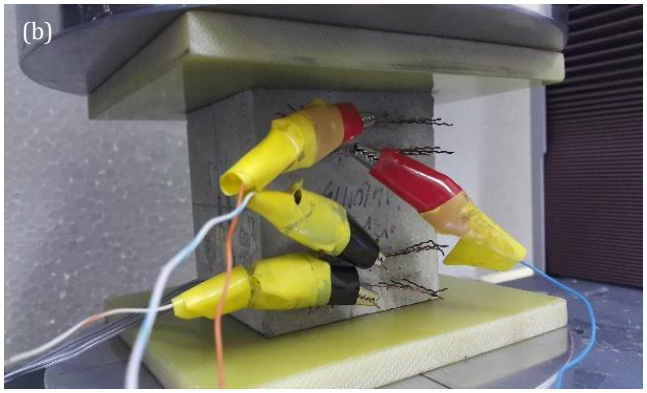

Fig. 2. (a) Test circuit; (b) The sample at test.

The resistance of the sample (R_s) at any time of the test were determined by using Ohms law as in Eq. (1).

$$R_s = \frac{V_s}{I_c}. \quad (1)$$

The percent change of the electrical resistance of the sample (%R) was determined by Eq. (2). R_{so} is electrical resistance of sample without load.

$$\%R = \left(\frac{R_s}{R_{so}} - 1\right) \times 100. \quad (2)$$

Performance measures were defined in this study. These are gage factor (K) and linearity (LE). Gage factor (K) is the change in electrical resistance per unit strain and determined by Eq. (3). The higher the gage factor, the more sensitive to strain the sensor is. Commercial strain gages have a gage factor of 2. Linearity (LE) is the percent of maximum difference (Δ_{max}) between input-output curve (%R versus strain curve) and fitted linear regression line, to full scale output (R_{fs}) as in Eq. (4). As the linearity decreases, the error in strain measurement decreases.

$$K = \frac{(R_s - R_{so})/R_{so}}{\Delta\varepsilon}, \quad (3)$$

$$\%LE = \left(\frac{\Delta_{max}}{\%R_{fs}}\right) \times 100. \quad (4)$$

3. Results and Discussion

In this study, six different mixtures were designed and tested with compression test. The relation between strain and electrical resistance change was determined.

The strain-%R graph of M0 is presented as shown in Fig. 3(a). M0 have a gage factor of K=21, linearity of LE=%15 and correlation coefficient is R^2=0.93. M0 is 10 times more sensitive than commercial strain gages while not having any fibers.

Br1 which has 0.35% fiber is almost 2.5 times more sensitive than M0 and almost 24 times more sensitive than commercial strain gages. It has gage factor of K=47, linearity of LE=6%. The change in electrical resistance had a strong linear relationship with strain with a correlation coefficient of 0.99 as shown in Fig. 3(b).

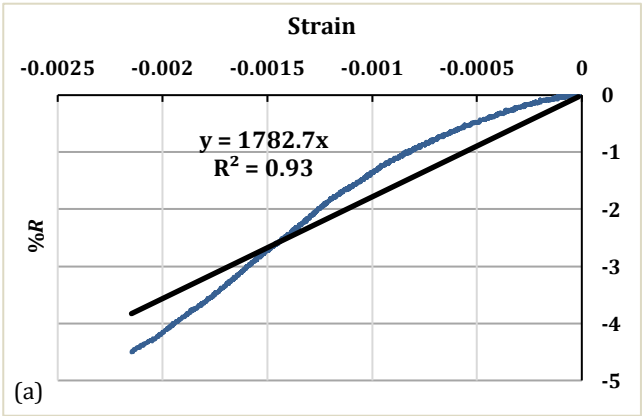

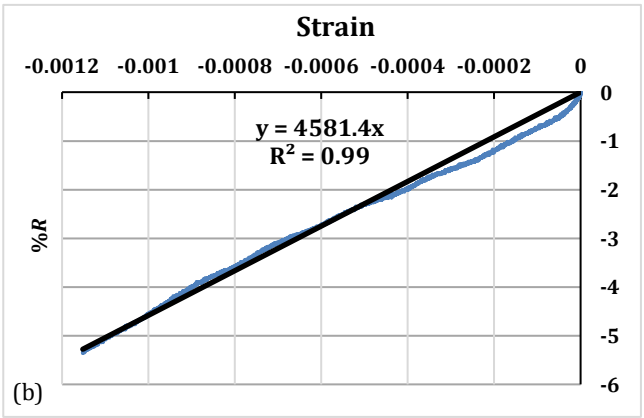

Fig. 3. Strain-the percent change of electrical resistance: (a) M0 mixture without fiber (K=21, LE=15%, R^2=0.93); (b) Br1 (0.35%) mixture (K=47, LE=6%, R^2=0.99).

Br2 having 0.5% brass fiber volume fraction has the gage factor of K=58, linearity of LE=8% as shown in Fig. 4(a).

The strong linear relationship between the changes in electrical resistance-strain had a correlation coefficient of 0.99. The gage factor of Br2 is almost 27 times more sensitive than commercial strain gages.

The mixture Br3 has 0.8% fiber volume fraction. It has gage factor of K=53, linearity of LE=3%. The correlation coefficient of best fit line to the data is 0.99 (Fig. 4(b)).

The mix Br4 having 1% brass fiber volume fraction has a gage factor of K=60, linearity of LE=6%. It is almost 30 times more sensitive than commercial strain gages. The correlation coefficient of fit line is R^2=0.99 (Fig. 5(a)).

The gage factor of Br5 having 1.5% brass fiber volume fraction is K=40, which is 20 times more sensitive than commercial metal strain gages. Br5 had a linearity of LE=5%. The electrical resistance change and strain has a correlation coefficient of 0.99 which testifies the strong linear relationship seen in Fig. 5(b).

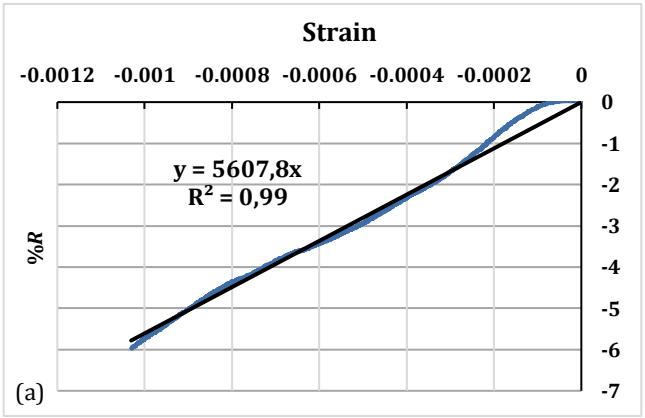

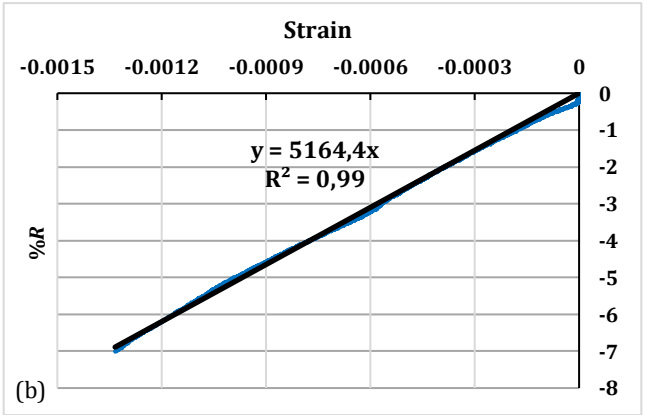

Fig. 4. Strain-the percent change of electrical resistance: (a) Br2 (0.5%) mixture (K=58, LE=8%, R^2=0.99); (b) Br3 (0.8%) mixture (K=53, LE=3%, R^2=0.99).

4. Conclusions

Six different brass fiber reinforced cement based concrete mixes were designed with different volume fraction of brass fiber. Three cube samples were cast and cured from each mix. Compression test was applied to each cube sample. Strain and electrical resistance was measured simultaneously. The relation between the changes in electrical resistance and strain were examined to evaluate the strain sensitivity of mixtures. The results obtained are as follows:

- Under compressive strain, micro crack and voids closed, fiber-matrix, fiber-fiber and matrix-matrix contact increased which led to decrease of electrical resistance.
- Tested brass fiber reinforced concrete mixes have higher strain sensitivity than metal foil strain gages. Gage factors as high as 60 were obtained for brass fiber reinforced concrete while metal foil strain gages had gage factor of 2.
- The brass fiber reinforced concrete had a strong linear relationship of strain – electrical resistance change.

- Brass fiber reinforced concrete mixes were more sensitive to strain than the concrete which did not have any brass fiber.

The results obtained in this study are important steps to develop smart concrete which senses its strain and damage.

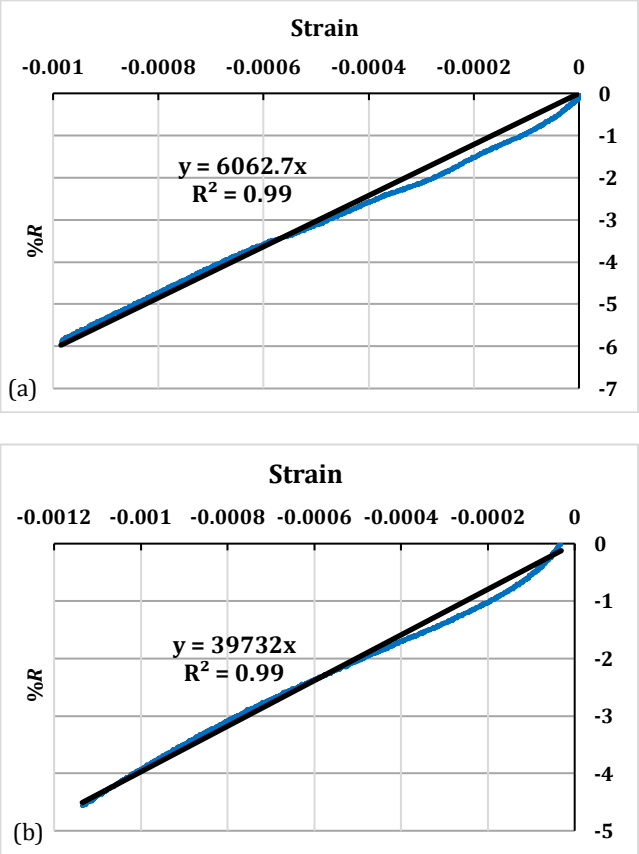

Fig. 5. Strain-the percent change of electrical resistance: (a) Br4 (1%) mixture (K=60, LE=6%, R^2=0.99); (b) Br5 (1.5%) mixture (K=40, LE=5%, R^2=0.99).

Acknowledgements

This work is supported by The Scientific and Technological Research Council of Turkey (TUBITAK) through Grant no: 213M452. The authors would like to thank to Batıbeton Batıçim West Anatolia Cement Industry Inc. for supplying cement and aggregate; Sika Construction Chemicals Co. for supplying super plasticizer; BASF Chemical Co. for supplying silica fume, BMS Metal Inc. for supplying brass fibers.

References

Chen B, Liu J (2008). Damage in carbon fiber–reinforced concrete, monitored by both electrical resistance measurement and acoustic emission analysis. *Construction and Building Materials,* 2, 2196-2201.

Chung DDL (1998). Self-monitoring structural materials. *Materials Science and Engineering,* 22(2), 57-78.

Chung DDL (2001). Functional properties of cement –matrix composites. *Journal of Materials Science,* 36, 1315-1324.

Chiarello M, Zinno R (2005). Electrical conductivity of self-monitoring CFRC. *Cement and Concrete Composites*, 27, 463-469.

Fu X, Ma E, Chung DDL, Anderson WA (1997). Self-monitoring in carbon fiber reinforced mortar by reactance measurement. *Cement and Concrete Research*, 27(6), 845-852.

Han B, Guan X, Ou J (2007). Electrode design, measuring method and data acquisition system of carbon fiber cement paste piezoresistive sensors. *Sensors and Actuators A:Physical*, 135(2) , 360-369.

Li H, Xiao H, Ou J (2006). Effect of compressive strain on electrical resistivity of carbon black-filled cement –based composites. *Cement and Concrete Composites,* 28(9), 824-828.

Li H, Xiao H, Ou J (2008). Electrical property of cement-based composites filled with carbon black under long-term wet and loading condition. *Composites Science. and Technology,* 68(9) , 2114-2119.

Reza F, Batson GB, Yamamuro JA, Lee JS (2003). Resistance changes during compression of carbon fiber cement composites. *Journal of Materials in Civil Engineering*, 15(5), 476-483.

Teomete E (2013). Relations of crack length and electrical resistance for smart cement based composites. *Cement Wapno Beton*, 18(6), 329-334.

Teomete E (2014). Transverse strain sensitivity of steel fiber reinforced cement composites tested by compression and split tensile tests. *Construction and Building Materials,* 55, 136-145.

Teomete E, Erdem TK (2011). Cement based strain sensor: A step to smart concrete. *Cement Wapno Beton*, 16(2), 78-92.

Teomete E, Kocyigit OI (2013). Tensile strain sensitivity of steel fiber reinforced cement matrix composites tested by split tensile test. *Construction and Building Materials*, 47, 962-968.